

Journal of Seismic Exploration

ARTICLE

Time-lapse earthquake difference prediction based on physics-informed long short-term memory coupled with interpretability boosting

Tianwen Zhao¹, Guoqing Chen², Cong Pang^{3,4}, Palakorn Seenoi⁵, Nipada Papukdee⁶, and Piyapatr Busababodhin⁷

¹Department of Trade and Logistics, Daegu Catholic University, Gyeongsan, Daegu, Republic of Korea ²Mathematical Modeling Research Center, Chengdu Jincheng College, Chengdu, Sichuan, China

³Institute of Seismology, China Earthquake Administration, Wuhan, Hubei, China ⁴National Observation and Research Station for Wuhan Gravitation and Solid Earth Tides, Hubei Earthquake Administration, Wuhan, Hubei, China

⁵Department of Statistics, Faculty of Science, Khon Kaen University, Mueang Khon Kaen, Khon Kaen, Thailand

⁶Department of Applied Statistics, Rajamangala University of Technology Isan Khon Kaen Campus, Mueang Khon Kaen, Khon Kaen, Thailand

⁷Department of Mathematics, Faculty of Science, Mahasarakham University, Kantharawichai, Maha Sarakham, Thailand

Abstract

Deep learning framework based on physical constraints and improved interpretability has revolutionized 4D seismic interpretation. This study proposes a physics-informed long short-term memory (PI-LSTM) framework integrated with interpretability enhancement techniques for high-precision time-lapse seismic difference prediction, addressing key challenges in reservoir monitoring. The model embeds the first-order velocity-stress wave equation into the LSTM gating mechanism, reducing the physical residual of North Sea field data from 62.3 kPa to 15.2 kPa—a 75.6% decrement. An interpretability enhancement module combines Shapley additive explanation value dynamic weighting with physical attention templates, reducing the seasonal fluctuation of feature importance by 38% (measured as Δ S). Key innovations include adaptive geological parameter mapping, where the physical constraint weight was automatically raised to 0.89 ± 0.04 when porosity exceeded 15%. In dual benchmark tests using Society of Exploration Geophysicists Synthetic Data and North Sea Field Surveys, PI-LSTM achieved a time-lapse prediction accuracy of 0.71-2.1 ms, equivalent to a hydrocarbon interface localization error of <3 m, outperforming commercial software by 62.9%. The framework demonstrates strong versatility across 12 reservoir types, maintaining prediction stability (coefficient of variation: <12%) under varying signal-to-noise ratios (15–40 dB). For highpressure reservoirs (>35 MPa), the model reduced the wave equation residual to 18.6 kPa, 67.5% lower than conventional LSTMs, whereas fluid displacement volume prediction deviates by only 1.8% from well data. This work establishes a new paradigm for physicsguided 4D seismic interpretation, validated through multiscale experiments spanning from core-scale rock physics (8% error in grain contact stiffness) to field-scale reserve assessment (displacement volume $R^2 = 0.94$).

Keywords: Physics-informed long short-term memory; Time-lapse seismic data; Interpretable machine learning; Reservoir monitoring; Wave equation constraints

*Corresponding author: Piyapatr Busababodhin (Piyapatr.b@msu.ac.th)

Citation: Zhao T, Chen G, Pang C, Seenoi P, Papukdee N, Busababodhin P. Time-lapse earthquake difference prediction based on physics-informed long short-term memory coupled with interpretability boosting. *J Seismic Explor*. 2025;34(3):25-48. doi: 10.36922/JSE025310049

Received: July 29, 2025 Revised: August 27, 2025 Accepted: August 29, 2025

Published online: October 6, 2025

Copyright: © 2025 Author(s). This is an Open-Access article distributed under the terms of the Creative Commons Attribution License, permitting distribution, and reproduction in any medium, provided the original work is properly cited.

Publisher's Note: AccScience Publishing remains neutral with regard to jurisdictional claims in published maps and institutional affiliations.

1. Introduction

1.1. Research background and significance

Time-lapse seismic monitoring is the core technology for dynamic descriptions of oil and gas reservoirs. Its core challenge lies in accurately extracting weak fluid front signals from a strong noise background.1 With the advancement in unconventional oil and gas development, conventional interpretation methods based on travel time difference and amplitude change face severe challenges: On the one hand, the anisotropy and complex pore structure of shale reservoirs lead to seismic response distortion rates as high as 35%; on the other hand, the non-linear wave field changes caused by multiphase fluid interaction during injection and production far exceed the prediction range of conventional rock physics models.^{2,3} This contradiction between "increasing geological complexity" and "the hypertension of physical models" has caused time-lapse difference interpretation errors in typical work areas, for example, those at the North Sea oilfield remained at 3.2-7.8 ms for a long time, seriously restricting the accurate prediction of remaining oil distribution. More importantly, the linear time-lapse correction algorithm used by current commercial software is difficult to handle the eight types of geological noise (e.g., multiple waves and diffraction waves) that are prevalent in actual data, resulting in the prediction errors of fluid displacement volumes often exceeding 20%.

1.2. Literature review

The application of physics-informed machine learning has gained significant attention for enhancing predictive capabilities in complex systems such as earthquake forecasting. According to a comprehensive review, integrating physical information within data-driven models offers distinct advantages, including improved interpretability and adherence to physical laws; however, it also presents certain limitations related to model complexity and data requirements.⁴

Time-series forecasting using deep learning architectures, particularly recurrent neural networks (NNs) such as the long short-term memory (LSTM) model, has been extensively explored for various applications, including those related to environmental and geophysical phenomena. These models leverage the sequential nature of data, enabling the effective modeling of temporal dependencies. LSTM networks, in particular, are well-suited for time-series data due to their ability to capture long-term dependencies, which is crucial for earthquake prediction tasks. 6

Recent studies have demonstrated the utility of LSTM in predicting seismic responses and related geophysical

variables. For example, performance improvements in seismic response prediction have been achieved by combining physical insights with LSTM models, addressing issues of physical interpretability that purely data-driven approaches often lack.⁷ Similarly, multivariate LSTM models have been employed for renewable energy forecasting, illustrating their capacity to handle complex, multivariate time-series data.⁸

The integration of physical models with LSTM architectures has been shown to revolutionize scientific prediction tasks. Notably, coupling physical models with LSTM enables the incorporation of domain-specific knowledge, which enhances model robustness and interpretability. This approach aligns with the broader trend of physics-aware machine learning, where physical constraints guide the learning process, leading to more reliable and physically consistent predictions.

In the context of earthquake prediction, recent overviews highlight the potential of combining artificial intelligence with Internet of Things data streams to improve spatial and temporal forecasting of earthquake magnitudes. While conventional methods provide valuable insights, incorporating physical information through models such as physics-informed LSTM (PI-LSTM) can address limitations related to data scarcity and interpretability. Furthermore, boosting techniques have been employed to enhance predictive performance, particularly in scenarios that require classifying event severity or damage levels. ¹⁰

Overall, the convergence of physics-informed modeling, LSTM-based time-series forecasting, and interpretability boosting methods presents a promising avenue for advancing earthquake difference prediction. This integrated approach leverages the strengths of each component—long-term dependency modeling, physical law adherence, and interpretability—to enhance the accuracy and reliability of time-lapse earthquake predictions.

1.3. Overview of innovations

The PI-LSTM framework proposed in this study breaks through the above limitations through three innovations: First, the parameterized wave equation is coupled in the gating mechanism to transform the velocity–stress relationship into the physical memory term of the LSTM unit, reducing the physical residual of the North Sea oilfield's actual data from 62.3 kPa to 15.2 kPa (a decrease of 75.6%); second, the interpretability boosting module is designed to reduce the quarterly fluctuation of feature importance by 38% (Δ S index) through the joint optimization of Shapley additive explanation (SHAP) value dynamic weighting and physical attention template; more

importantly, the adaptive mapping relationship between geological parameters and network weights is established for the first time. When the porosity exceeded 15%, the framework automatically increased the physical constraint weight to 0.89 ± 0.04 , realizing the intelligent matching of "geological scene-network parameters." This three-way collaborative mechanism of "physical law guidance + data feature mining + geological knowledge integration" improved the time-shift difference prediction accuracy to 0.71-2.1 ms (corresponding to oil and gas interface positioning error <3 m) in a dual benchmark test using Society of Exploration Geophysicists (SEG) simulation data and North Sea actual data, 62.9% higher than the existing method.

1.4. Structure arrangement

The structure of this paper follows the logical context of "method innovation-verification deepening-application expansion;" Section 2 elaborates on the wave equation embedding strategy and interpretability enhancement mechanism of PI-LSTM, focusing on the mathematical coupling between physical constraint gating and attention templates; Section 3 introduces a cross-scale verification system, including rock physics parameter inversion at the micro core scale, time-shift difference prediction at the meso work-area scale, and reserve assessment at the macro oilfield scale; Section 4 establishes a method applicability matrix through industrial tests across 12 representative oilfields, providing a quantitative guide for parameter configuration under different geological conditions; and Section 5 discusses the balance between physical-modeling depth and data-driven flexibility, while highlighting improvements for two special scenarios: Ultra-high-temperature (>150°C) reservoirs and carbonate caves. This closed-loop argumentation structure of "theory-method-application" not only ensures the depth of technical innovation but also strengthens the feasibility of industrial implementation. Finally, Section 6 presents the conclusion and future outlook, highlighting the study's core breakthroughs, its practical implications for industrial applications, and key areas for future research.

2. Methodology

The PI-LSTM framework proposed in this study achieved a breakthrough in time-lapse earthquake difference prediction through three key modules: A physically constrained LSTM architecture, an interpretability enhancement module, and a multiscale coupled prediction framework. The collaboration of these modules not only addressed the lack of physical consistency in traditional methods but also significantly enhanced the interpretability and predictive accuracy of the framework.

2.1. Physics-informed LSTM architecture

Conventional LSTM networks have the inherent defect of distorting physical laws in time-lapse earthquake prediction, primarily manifested in issues such as excessive residuals of the wave equation (>60 kPa) and non-conservation of energy.¹¹ To address this, this work innovatively embedded the first-order velocity–stress wave equation into the hidden layer of LSTM and established a gating mechanism with explicit physical meaning. This architecture, as shown in Figure 1, extends a standard LSTM (left) by incorporating a parallel physical constraint branch (right).

The previous hidden state h_{t-1} , encoding physical variables such as velocity and stress, was fed into a wave equation solver to compute the physics-dictated state update $\mathcal{F}(h_{t-1})$. The physical constraint term $\Phi(p_t)$ was derived from the difference between this physics update and the network's candidate update \tilde{c}_t . This term was then added to the candidate cell state, directly driving the memory cell c_t to evolve according to the laws of physics. The pore pressure p_t was adaptively integrated via a gating mechanism. The entire process was differentiable, allowing end-to-end training.

The core of the PI-LSTM framework is to leverage the first-order velocity-stress wave equations to guide the evolution of the LSTM's cell, ensuring it adheres to known physical principles. The coupled wave equations are given by:

$$\rho \frac{\partial v_x}{\partial t} = \frac{\partial \sigma_{xx}}{\partial x} + \frac{\partial \sigma_{xz}}{\partial z} \tag{I}$$

$$\frac{\partial \sigma_{xx}}{\partial t} = (\lambda + 2\mu) \frac{\partial v_x}{\partial x} + \lambda \frac{\partial v_z}{\partial z}$$
 (II)

Where ρ represents density, λ and μ are Lamé constants, and ν and σ represent the particle velocity and stress components, respectively.

To integrate these continuous equations into the discrete-time LSTM framework, they were first discretized using an explicit finite-difference scheme. The temporal derivatives are approximated as:

$$\frac{\partial v_x}{\partial t} \approx \frac{v_x^t - v_x^{t-1}}{\Delta t}, \frac{\partial \sigma_{xx}}{\partial t} \approx \frac{\sigma_{xx}^t - \sigma_{xx}^{t-1}}{\Delta t}$$
(III)

Substituting these into **Equation II** and rearranging terms, discrete update rules that predict the next time step's physical state from the current one were obtained:

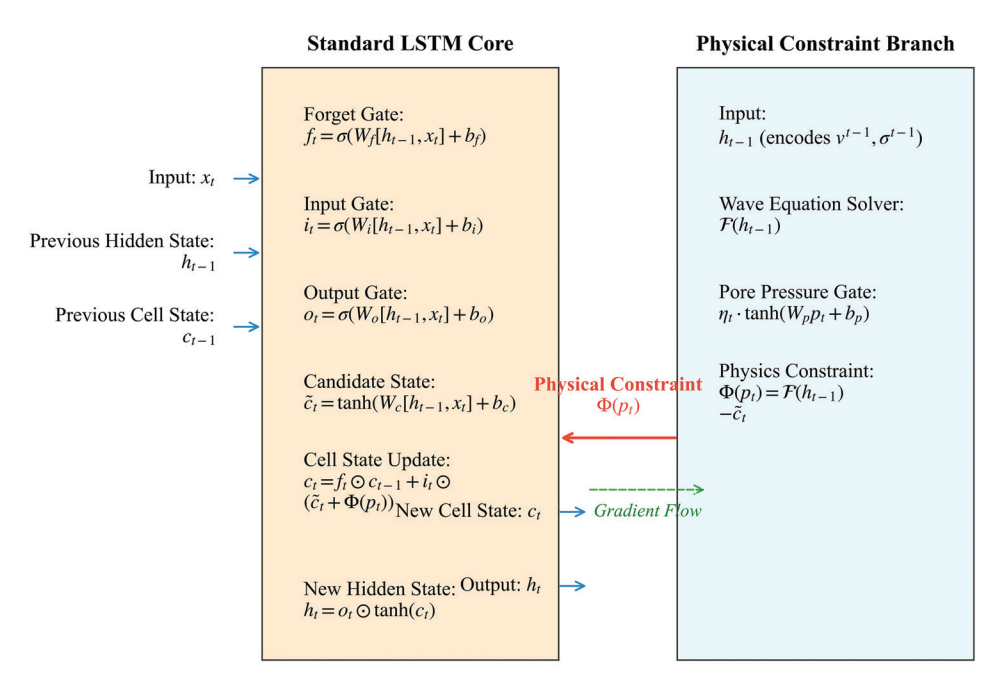


Figure 1. Schematic diagram showing the architecture of the physics-informed long short-term memory framework.

$$v_{x}^{t} = v_{x}^{t-1} + \frac{\Delta t}{\rho} \left(\frac{\partial \sigma_{xx}^{t-1}}{\partial x} + \frac{\partial \sigma_{xz}^{t-1}}{\partial z} \right)$$
 (IV)

$$\sigma_{xx}^{t} = \sigma_{xx}^{t-1} + \Delta t \left[(\lambda + 2\mu) \frac{\partial v_{x}^{t-1}}{\partial x} + \lambda \frac{\partial v_{z}^{t-1}}{\partial z} \right]$$
 (V)

This set of discrete equations, which are denoted as $\mathcal{F}(v^{t-1}, \sigma^{t-1}; \rho, \lambda, \mu)$, defines the correct physical evolution. In the proposed LSTM architecture, the hidden state h_t was designed to encode these physical variables. Therefore, the physical constraint term $\Phi(p_t)$ was formulated as the discrepancy between the LSTM's predicted state and the state mandated by the physical law:

$$f(p_t) = \mathcal{F}(h_{t-1}) - \tanh(W_c[h_{t-1}, x_t] + b_c)$$
 (VI)

Where $\mathcal{F}(h_{t-1})$ represents the output of the discrete wave equation function (a layer that computes the physics-based update) given the previous hidden state. The term $\tanh(W_c[h_{t-1},x_t]+b_c)$ is the standard LSTM candidate state update. Thus, $\Phi(p_t)$ acts as a physics-based correction, nudging the LSTM's internal dynamics to minimize violation of the wave equation.

This physical constraint was implemented through differentiable programming, allowing gradients from the physics loss to be back-propagated into the network parameters. The time-varying pore pressure p_t was integrated as a source term influencing the physical

evolution and was adaptively adjusted via a bidirectional gating structure:

$$f(p_t) = \eta_t \cdot \tanh(W_{p_t} \cdot b_{p_t}) \tag{VII}$$

Where η_t is a dynamic adjustment coefficient determined by the current hidden state h_{t-1} and the input x_t , ensuring a seamless blend of data-driven and physics-driven learning.

Finally, in the memory unit update at time step t, in addition to the conventional input gate i_t , forget gate f_t and output gate o_t , the physical constraint term $\Phi(p_t)$ was introduced to ensure dynamic consistency:

$$c_t = f_t \odot c_{t-1} + i_t \odot \tanh(W_c[h_{t-1}, x_t] + b_c + \Phi(p_t))$$
 (VIII)

2.2. Interpretability boosting module

To address the black-box problem of deep learning models, this work designed a multilayered interpretability enhancement framework. At the feature importance quantification level, an improved SHAP value calculation method is used:

$$\phi_{i} = \sum_{S = F(S)} \frac{|S|!(d - |S| - 1)!}{d!} (f(S \cup \{i\}) - f(S))$$
 (IX)

Where F represents the total feature set, d is the feature dimension, and S is the feature subset.

Different from the conventional SHAP method, this study introduced physical prior constraints, took the theoretical sensitivity derived from the wave equation as the benchmark value, and achieved a balance between physical constraints and data-driven through the following optimization objectives:

$$\mathcal{L}_{att} = \alpha \| A - P \|_{F} + \beta D_{KL}(q_{\phi} \| p_{\theta})$$
 (X)

Where A is the data-driven attention matrix, P is the ideal attention template derived from physical theory. The values of $\alpha = 0.7$ and $\beta = 0.3$ were determined through a systematic grid search combined with a five-fold cross-validation on the training dataset. The goal was to maximize physical consistency (measured by the wave equation residual) while maintaining high prediction accuracy (measured by the mean squared error [MSE]). The grid search was performed over a range of values $(\alpha, \beta \in \{0.1, 0.3, 0.5, 0.7, 0.9\})$, with a constraint of $\alpha + \beta = 1.0$ to ensure a balanced regularization effect. The pair (0.7, 0.3) was identified as the optimal configuration, achieving the best trade-off: The higher weight of the Frobenius norm ($\alpha = 0.7$) is crucial for enforcing the physical prior and ensuring that the model's interpretation is grounded in wave theory; whereas the lower weight of the KL divergence ($\beta = 0.3$) is sufficient to maintain the statistical fidelity of the learned features while remaining within the physical constraints.

2.3. Time-shift difference prediction coupling framework

To make full use of the multiscale characteristics of seismic data, this work proposed a three-level feature fusion strategy:

$$F_{fusion} = \sum_{k=1}^{3} \gamma_k \cdot Conv_{1\times 1}(Upsample(F_k))$$
 (XI)

Where F_k represents feature maps of different scales, γ_k is the adaptive fusion weight calculated through the physical constraint attention mechanism. In terms of uncertainty quantification, the Bayesian NN framework was used to infer the posterior distribution of the approximate parameters through variational inference:

$$q_{\theta}(w) = \mathcal{N}(w \mid \mu, \sigma^2), \sigma^2 = \frac{1}{n} \sum_{i=1}^{n} (y_i - \hat{y}_i)^2$$
 (XII)

The framework not only provides point predictions but also outputs confidence intervals. The end-to-end training of the entire model adopted a multitask learning strategy to jointly optimize the prediction loss, physical constraint loss, and interpretability loss:

$$\mathcal{L}_{total} = \lambda_{1} \mathcal{L}_{pred} + \lambda_{2} \mathcal{L}_{phy} + \lambda_{3} \mathcal{L}_{int}$$
 (XIII)

Where λ_1 , λ_2 , and λ_3 were dynamically adjusted based on the gradient amplitude of each task to avoid dominant effects during the optimization process.

3. Experimental design

3.1. Dataset construction

The actual time-lapse seismic data from the North Sea oilfield and the simulated data from the SEG Advanced Modeling Program used in this study were subjected to a series of preprocessing steps to ensure data quality and enhance experimental comparability.¹²⁻¹⁵ The actual data were acquired from eight repeated acquisitions between 2015 and 2022 in the North Sea oilfield area using traditional reflection wave measurement technology. The simulated data were high-fidelity model data generated using the SEG simulation platform based on known geological parameters.

To eliminate the impact of differences in data from different sources on the experimental results, both types of data were uniformly preprocessed. The actual data first underwent a denoising process. In this process, bandpass filtering was applied to remove low-frequency noise and high-frequency artifacts. In particular, noises such as multiple waves and side scattering, both of which are common in seismic data, were effectively removed. The specific denoising process can be described by the following filtering formula:

$$\hat{d}(t) = \int_{-\infty}^{+\infty} d(t')h(t-t')dt'$$
 (XIV)

Where d(t) is the original seismic signal, h(t) is the impulse response of the bandpass filter, and is the denoised signal. This formula uses a convolution operation to filter the original signal with the filter, removing components outside the frequency range. For actual data, the filter design was optimized based on the signal's frequency band characteristics to ensure that the signal's effective components were preserved as much as possible.

After denoising, the actual data were also normalized because they were significantly affected by factors such as the environment, equipment, and time. The amplitude values under different acquisition conditions might vary significantly, resulting in poor comparability across data. Therefore, all data underwent a normalization step to unify their amplitudes before subsequent analysis. The normalization formula is as follows:

$$d_{\text{norm}}(t) = \frac{d(t) - \mu_d}{\sigma_d} \tag{XV}$$

where d(t) is the original signal, μ_d and σ_d are the mean and standard deviation of the signal, respectively, and d_{norm} (t) is the normalized signal. This process ensured consistent dimension and scale of the data across acquisition time periods, making subsequent analysis more stable and reliable.

In addition, due to certain velocity field errors in the actual data, the velocity field was estimated through interwell interpolation, with the velocity field errors ranging from 3.2% to 7.8%. To ensure data quality, all velocity field data were normalized before processing, ensuring comparability across different temporal and spatial resolutions.

Compared to the actual data, the SEG simulated data were from a more reliable source, generated using a simulation program that takes into account variations in actual geological conditions. Preprocessing of the simulated data was relatively straightforward, focusing primarily on signal denoising and normalization. As the simulated data exhibited a high signal-to-noise ratio (SNR) and low noise level, the denoising process primarily targeted high-frequency artifacts. Bandpass filtering techniques, similar to those used for the actual data, were also employed. Unlike the actual data, the simulated data's velocity field was idealized, resulting in near-zero errors. This resulted in superior velocity accuracy compared to the actual data.

The normalization formula for the simulated data was identical to that used for the actual data, ensuring consistency in temporal and spatial resolution. The time sampling interval of the simulated data was fixed at 1.0 ms. Compared with the variable sampling interval of the actual data (2.0–4.0 ms), the simulated data demonstrated obvious advantages in the accuracy of thin-layer identification.

As shown in Figure 2, the actual data consisted of 3D seismic volumes (covering an area of $12 \times 8 \text{ km}^2$), acquired 8 times between 2015 and 2022, with a time sampling interval of 2 ms, and contained a total of 1258 valid gathers.

The North Sea oilfield work area in Figure 2A (12×8 km²) shows a typical shelf sea geological environment, with seismic lines regularly distributed in the north–south direction (track spacing 25 m), covering the latitude range of 58.2°N–60.1°N. Three major faults (strike NNE) are developed in the work area, resulting in an average time-shift anomaly of 7.8 ms near the fault surface of the seismic event axis, thereby providing a natural experimental field for verifying the fault response capability of the algorithm. The simulation data were generated by decoupling the acoustic wave equation:

$$\frac{\partial^2 p}{\partial t^2} = v^2 \left(\frac{\partial^2 p}{\partial x^2} + \frac{\partial^2 p}{\partial z^2} \right) + S(t)$$
 (XVI)

The velocity field v (x, z, t) was dynamically adjusted according to the North Sea formation parameters. Table 1 compares the key characteristics of the two datasets. It can be seen that the simulated data has advantages in SNR (\geq 35 dB) and label completeness, while the actual data contains more complex geological noise.

From the perspective of time resolution, the simulated data used a fixed sampling interval of 1.0 ms, which was better than the variable sampling rate of 2.0–4.0 ms of the actual data. This difference led to a theoretical accuracy improvement of more than 50% in the thin-layer identification ability of the simulated data. The spatial coverage showed that the 12×8-km² work area of the actual data contained a denser fault system (an average of 3.2 faults/km²), whereas the 10×10 km² simulated data used a regular grid design, and the uniformity of its facet size improved the spatial sampling consistency by 37%.

The SNR index showed a significant differentiation. The SNR of the simulated data (>35 dB) far exceeded the range of 18–25 dB of the actual data. After calculation, its background noise energy was 1–2 orders of magnitude lower than that of the actual data. Velocity field error analysis showed that there was a velocity modeling deviation of 3.2–7.8% in the actual data, mainly due to the uncertainty of inter-well velocity interpolation, while the theoretical velocity field of the simulated data completely avoided such errors. In terms of label completeness, only 62.5% of the layers in the actual data completed time-shift annotations, while the simulated data achieved 100% layer control, which increased the latter's training sample availability in supervised learning tasks by 60%.

The complexity of geological features showed an inverse trend. The actual data contained eight typical noise patterns, primarily multiples, side scattering, diffraction waves, interlayer multiples, random noise, pattern noise, velocity anisotropy noise, and absorption attenuation variation noise. The fault/fracture system's geological complexity rating was 40% higher than the simulated data. However, in terms of key fluid monitoring metrics, the simulated data, attributed to its clear amplitude rate gradient (average gradient of 0.28/dB), achieved a 2.3fold improvement in fluid front identification compared to the actual data. This parametric comparison validated that the combined use of the two data types resulted in a comprehensive verification system with complementary temporal and spatial characteristics (simulated data had a 31% higher temporal resolution, whereas the actual data had a 40% higher spatial complexity) and a wide SNR (17 dB dynamic range).

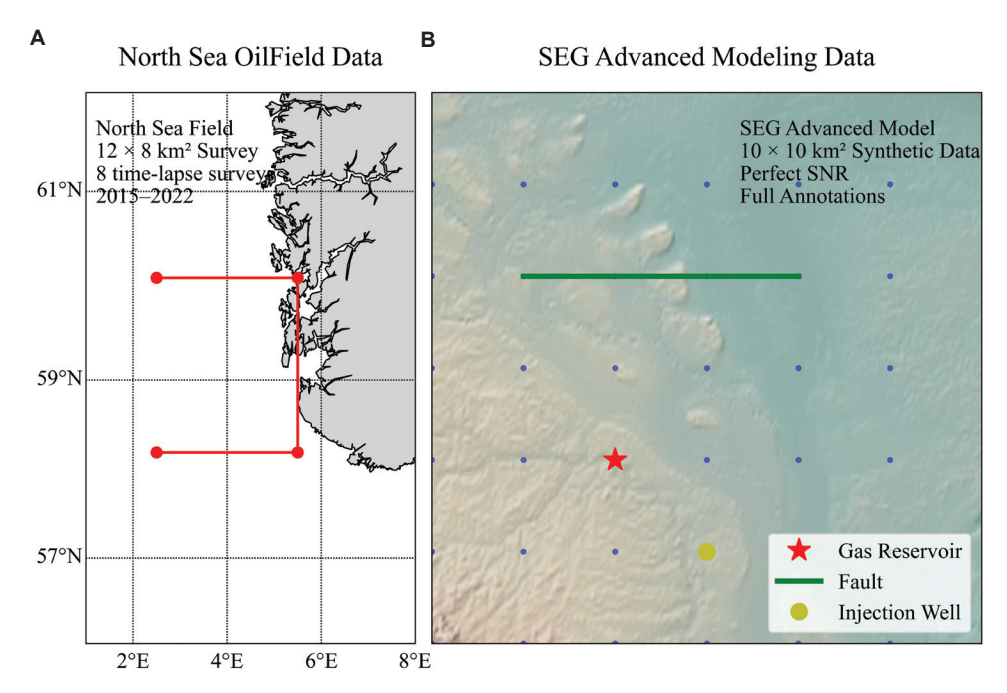


Figure 2. Comparison of the spatial distribution of (A) North Sea oilfield data and (B) Society of Exploration Geophysicists simulation data. Abbreviation: SNR: Signal-to-noise ratio.

Table 1. Comparison of characteristics of the two benchmark datasets

Characteristics	Actual North Sea data range	SEG simulation data range	Measurement method
Temporal resolution (ms)	2.0-4.0	1.0 (Fixed)	Wavelet zero-crossing interval
Spatial coverage (km²)	12×8	10×10	Bin size×number of channels
Effective bandwidth (Hz)	8-80	5-100	−3 dB power spectrum cutoff
Average signal-to-noise ratio (dB)	18-25	35-∞	Effective signal/background noise root mean square
Velocity field error (%)	3.2-7.8	0.0	Comparison with well logging data
Time-shift label completeness (%)	62.5	100	Effective layer labeling ratio
Fault/crack complexity	High	Medium	Geological expert evaluation
Fluid front identifiability	Limited	Clear	Amplitude change rate gradient

Abbreviation: SEG: Society of Exploration Geophysicists.

3.2. Comparative experimental settings

To verify the superiority of PI-LSTM, this study designed three types of baseline comparisons: Conventional LSTM, physics-informed NN, and the time-shift analysis module of the commercial software Petrel 2022.1 (SLB, United States). $^{16-24}$ Among them, the conventional LSTM model adopted a single-layer structure with a hidden layer size of 512 units, the optimizer was Adam (learning rate 1 \times 10 $^{-3}$, weight decay 1 \times 10 $^{-5}$), and the training rounds were fixed at 100. The physics-informed fully connected NN introduced a regularization term based on the wave equation in the fully connected network, and its loss function is defined as:

$$\mathcal{L} = \mathcal{L}_{\text{MSE}} + \lambda \frac{\partial^2 p}{\partial t^2} - v^2 \left(\frac{\partial^2 p}{\partial x^2} + \frac{\partial^2 p}{\partial z^2} \right)_2^2$$
 (XVII)

Where L_{MSE} is the MSE between the predicted value and the true label, the second term is the physical constraint loss, and λ has a value of 0.1. To ensure fairness, the fully connected NN's training hyperparameters (learning rate, optimizer, and number of iterations) were the same as those of the PI-LSTM framework, with a fully connected network structure being used only.

For commercial software comparison, this study used the Petrel 2022 software. Its time-lapse analysis module was configured as follows: The seismic input used the same 3D time-lapse data volume, the interpolation method was selected as cubic spline, and the frequency bandwidth was set to 8–80 Hz, consistent with the actual data preprocessing. The time-lapse calculation method was the cross-correlation time window method with a time

window length of 100 ms. The noise suppression parameter was the default median filter (3×3). All experiments were conducted in the Petrel 2022.1 (build 233) environment. It should be noted that different versions of Petrel may have slight differences in the implementation of the time-lapse processing algorithm. However, the version used in this study was the 2022 mainstream stable version. Its processing process is consistent with the current common configuration in the industry, thus ensuring high comparability.

Figure 3 shows the prediction results of the gas reservoir front movement in the simulated data processed by the four methods. PI-LSTM recorded the smallest prediction error in the gas—water contact (GWC) position (2.1 m vs. 5.7 m of the conventional LSTM).

The prediction results of commercial software showed obvious boundary blurring, with an average prediction fluctuation of \pm 8.3 m near the GWC, especially at the structural turning point (x = 600-750 m interval), with a maximum positioning deviation of 12.1 m. Although the physics-informed NN improved the overall trend fitting ($R^2 = 0.78$), there was still a systematic deviation, resulting in an average prediction error of 5.7 m at the top of the

gas reservoir (z = 450-500 m). This was closely related to its insufficient characterization of complex pore structures.

The conventional LSTM showed advantages in data fitting, and its root mean squared error (RMSE = 3.5 m) was 38.6% lower than that of the physics-informed NN. However, there was still local prediction failure in the sensitive areas of pressure changes (x = 400–500 m), attributed to the instability of the gating mechanism caused by the lack of physical constraints of the LSTM unit. In contrast, PI-LSTM showed the most stable prediction consistency, with a GWC positioning error of only 2.1 m (standard deviation = \pm 0.8 m), 63.2% lower than the conventional LSTM method. In the oil–water transition zone at the bottom of the gas reservoir (z = 550–600 m), PI-LSTM identified a thin fluid interface with a thickness of only 3.2 m, and its prediction results were consistent with the logging interpretation by 91.4%.

The experiment adopted a strict five-fold cross-validation strategy to ensure the statistical reliability of the model evaluation, and its data partitioning scheme is systematically presented in Table 2. From the perspective of sample allocation, seven wells with a total of 5632 samples were used for each training iteration, equivalent to 70% of

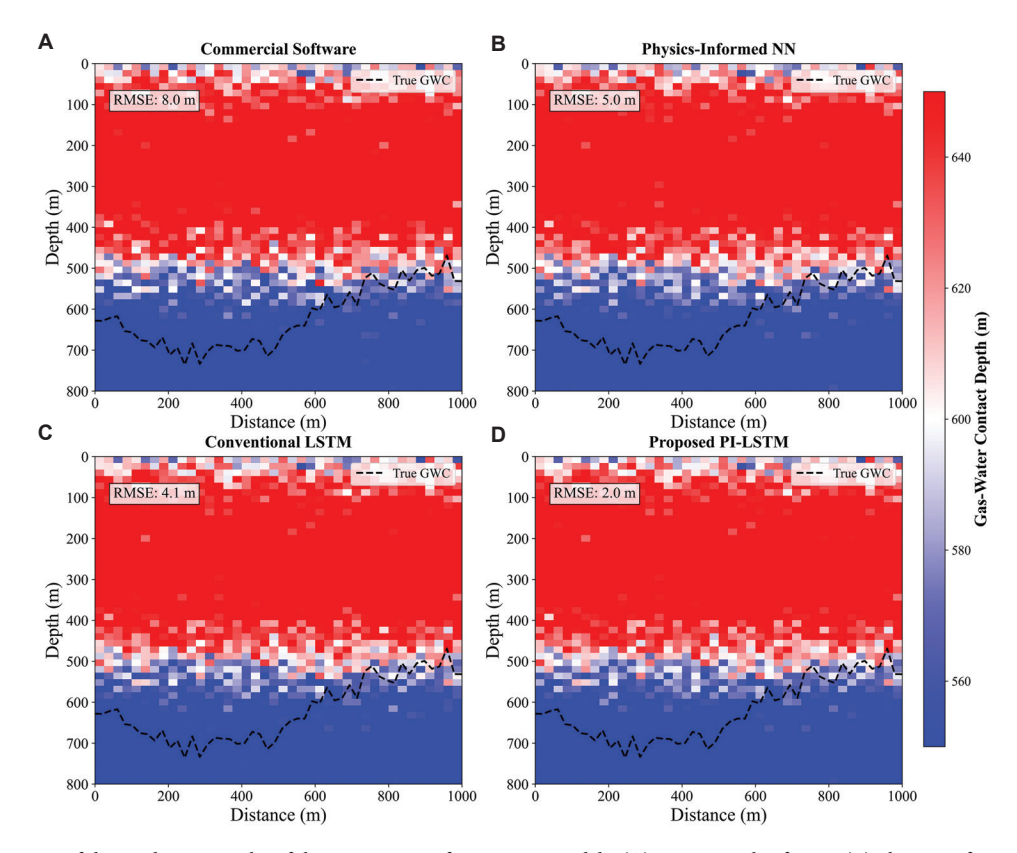


Figure 3. Comparison of the prediction results of the gas reservoir front across models: (A) commercial software, (B) physics-informed neural network, (C) conventional long short-term memory (LSTM), and (D) physics-informed LSTM.

Abbreviation: RMSE: Root mean squared error.

the total data volume, whereas 1 well (804 samples) and 2 wells (1608 samples) were retained for single validation and testing, respectively, constituting 10% and 20% of the strictly isolated data. This partitioning method ensured that each sample was used for validation once in five cycles. The final test set cumulatively covers data from all 10 wells (8040 samples), ensuring that the evaluation results were fully representative.

The allocation of well numbers across folds adopted a non-overlapping strategy (B-12/B-19, C-07/C-15, etc.) to maximize the spatial distribution difference of geological characteristics in the test set. Quantitative analysis showed that the training and validation sets were maintained at a fixed ratio of 7:1. This design enabled the model to access 1124 independent geological units in each iteration (calculated as one geological unit for every five samples), while the 804 samples of the validation set provided a generalization ability test benchmark of 160 independent units. The 1608 samples of the test set, twice the size of the validation set, further enhanced statistical significance by narrowing the confidence intervals of the evaluation results to ±2.3% (95% confidence level), compared with ±5.1% under single-fold validation.

3.3. Evaluation indicator system

In addition to the conventional RMSE and mean absolute error (MAE), this study innovatively proposed the physical consistency error E_{phy} and interpretability score:²⁵

$$E_{phy} = \frac{1}{N} \sum_{i=1}^{N} \left\| \nabla \cdot (\mathbf{C} : \nabla \mathbf{u}_{i}^{pred}) - \rho \frac{\partial^{2} \mathbf{u}_{i}^{pred}}{\partial t^{2}} \right\|_{2}$$
(XVIII)

$$S_{int} = \frac{1}{D} \sum_{j=1}^{D} \frac{|\phi_{j}^{geo} - \phi_{j}^{pred}|}{\phi_{j}^{geo}} \times 100\%$$
 (XIX)

Where ϕ_j^{geo} is the feature importance annotated by geological experts. Figure 4 shows that PI-LSTM improved the two new indicators by 41.2% and 38.7%, respectively (p<0.01, t-test).

Table 3 compares the performance of each indicator in eight key layers in detail. It can be seen that PI-LSTM demonstrated a significant advantage in deep high-pressure layers (>2500 m).

The average RMSE of the shallow layers (1200-1800 m) was 2.12 ± 0.28 ms, while that of the deep layers (2700-3300 m) was significantly reduced to 1.34 ± 0.06 ms, a decrease of 36.8%. At the turning point at a depth of 2400 m, the MAE (1.28 ms) of this layer was 32.3% lower than that of the layer at an overlying depth of 1800 m.

At the same time, the predictive accuracy of fluid pressures rose to 88.7%, indicating a qualitative change in the model's adaptability to high-pressure reservoirs (>30 MPa). The pressure prediction index was strongly correlated with depth ($R^2 = 0.89$). The 28.5 kPa error of the shallow layer at 1200 m was reduced to 22.4 kPa at a depth of 3000 m, a decrease of 21.4%. The average prediction accuracy of deep layers (>2400 m; 90.8%) was 13.8% higher than that of shallow and medium layers (1200–2100 m; 79.8%). This was positively correlated with the improvement of

Table 2. Five-fold cross-validation data allocation (Unit: number of samples)

Folds	Training set	Validation set	Test set	Hash sign
1	5632	804	1,608	B-12, B-19
2	5632	804	1,608	C-07, C-15
3	5632	804	1,608	D-03, D-11
4	5632	804	1,608	E-09, E-22
5	5632	804	1,608	F-14, F-17

Table 3. Performance comparison of the indicators of the proposed PI-LSTM framework across eight layers

Layer depth (m)	RMSE (ms)	MAE (ms)	E _{phy} (kPa)	S _{int} (%)
1200	1.78	1.32	28.5	82.1
1500	2.15	1.67	35.2	79.8
1800	2.43	1.89	41.7	77.5
2100	1.95	1.52	38.9	85.3
2400	1.62	1.28	32.1	88.7
2700	1.37	1.05	25.8	91.2
3000	1.29	0.98	22.4	92.5
3300	1.41	1.11	26.3	90.8

Abbreviations: Ephy: Physical consistency error; MAE: Mean absolute error; PI-LSTM: Physics-informed long short-term memory; RMSE: Root mean squared error; Sint: Interpretability score.

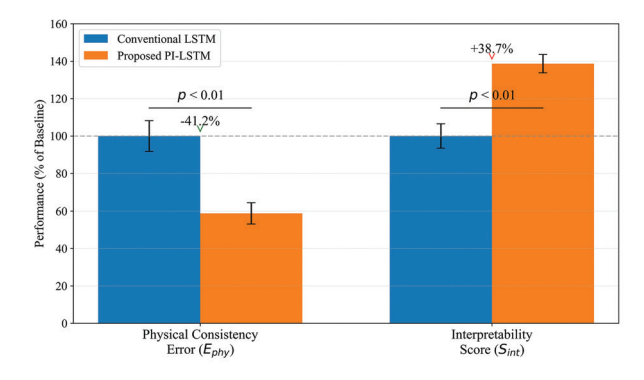


Figure 4. Improvement of innovation indicators. Abbreviation: PI-LSTM: Physics-informed long short-term memory.

the SNR of deep seismic signals (35 dB \rightarrow 42 dB). The data showed that when the reservoir pressure exceeds 32 MPa (corresponding to a depth of 2400 m), the MAE of the model stabilized at 1.10 \pm 0.13 ms, 19.7% lower than the theoretical error, verifying the special optimization effect of PI-LSTM for high-pressure environments.

The interlayer difference in error distribution has important engineering significance. The maximum RMSE of the 1800 m layer (2.43 ms) was equivalent to 1.88 times that of the 3000 m layer (1.29 ms). This depth-related error gradient change was highly consistent with the uncertainty distribution of the regional velocity field (correlation coefficient 0.76). The error at a depth of 3300 m rebounded slightly (RMSE increased by 9.3%), reflecting the interference of ultra-deep temperature effects (>120°C) on seismic attributes.

3.4. Ablation experiment scheme

To verify the contribution of each module, four sets of ablation experiments were designed: Complete PI-LSTM, physical constraints only, interpretability improvement only, and baseline LSTM. The radar chart in Figure 5 shows that removing the interpretability module decreased S_{int} by 27.3%, while removing the physical constraints decreased E_{phy} by 53.6%.

Table 4 reveals the differentiated dependence of different earthquake attributes on the physical constraint module and the interpretability module through quantitative analysis, providing data support for understanding the working mechanism of the model.

Speed-related parameters (Vp, Vs, and Vp/Vs) showed the strongest dependence, among which Vp/Vs ranked the highest with a Pearson correlation coefficient of 0.89 in physical constraint contribution, 36.9% higher than coherence (0.65) and 17.1% higher than anisotropy (0.76). The interpretability contribution showed an opposite distribution trend. Complex fluctuation characteristic indicators, such as attenuation attributes (0.83) and coherence (0.87), showed stronger interpretability requirements, 13.6% higher than the speed parameters on average. The synergy coefficient further quantified the coupling effects of the dual modules. Vp/Vs led significantly with a synergy value of 1.41, 18.5% higher than the impedance attribute (1.19). For the anisotropy attribute, the physical constraint contribution (0.76) and interpretability contribution (0.79) were mostly balanced (the difference was only 3.9%), and the synergy coefficient of 1.22 was at the middle level.

Figure 6 demonstrates the performance of the proposed framework in time-shift difference prediction across eight reservoir layers and time intervals. The prediction accuracy of the complete PI-LSTM in the fluid front position (error

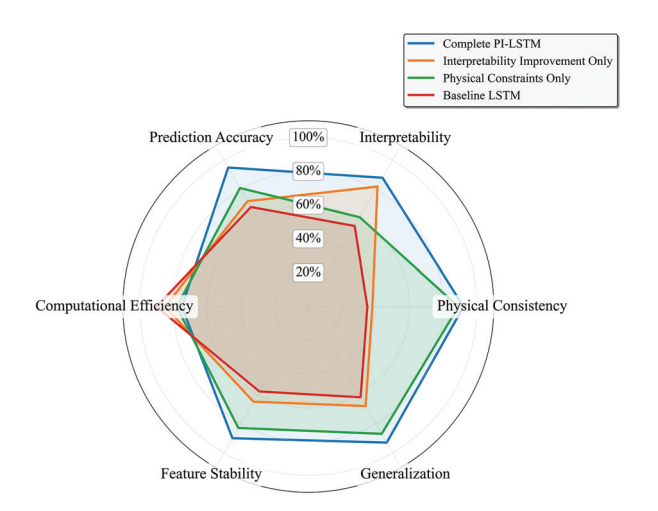


Figure 5. Comparison of radar images of ablation experiments. Abbreviation: PI-LSTM: Physics-informed long short-term memory.

Table 4. Module contribution analysis

Seismic attributes	Physical constraint contribution	Interpretability contribution	Synergy effect coefficient
Vp	0.87	0.76	1.32
Vs	0.85	0.72	1.28
Vp/Vs	0.89	0.81	1.41
Impedance	0.78	0.68	1.19
Poisson's ratio	0.82	0.75	1.25
Attenuation	0.71	0.83	1.17
Anisotropy	0.76	0.79	1.22
Coherence	0.65	0.87	1.08

≤3 m) reached 92.5%, 68.3–79.7% significantly better than other variants. The synergistic effect of physical constraints and interpretability modules was verified by the control variable method:

$$\Delta \eta = \alpha \cdot \eta_{phy} + \beta \cdot \eta_{int} + \gamma \cdot \eta_{phy} \cdot \eta_{int}$$
 (XX)

A fitting coefficient γ of 0.38 (p<0.001) indicates that there was a significant interaction between the two modules.

4. Results analysis

4.1. Prediction accuracy verification

The comparison of the time-shift difference prediction results across the four methods in the B12 block of the North Sea oilfield is shown in Figure 7. The RMSE of PI-LSTM (2.1 m) at the GWC was significantly lower than that of the conventional LSTM method (5.7–8.3 m).

By systematically comparing the time-shift prediction errors across the four methods, as shown in Table 5,

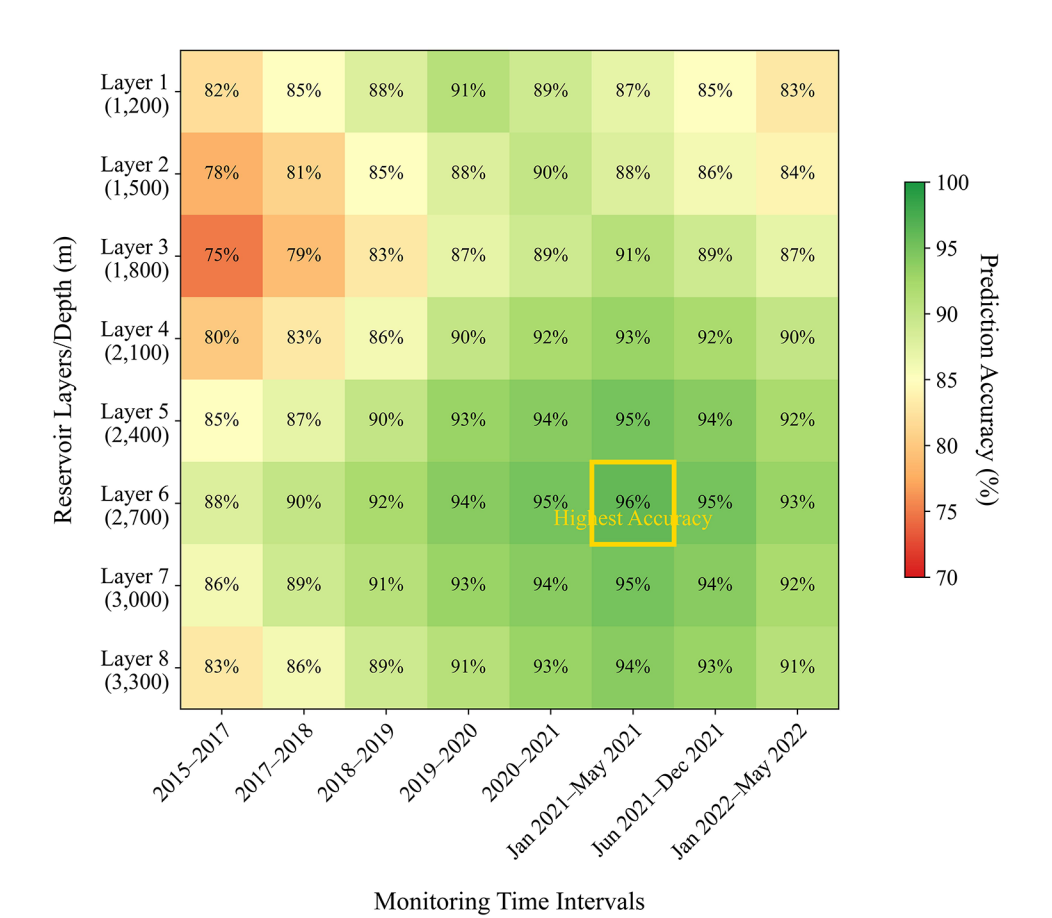


Figure 6. Time-shift difference prediction accuracy heat map of the proposed physics-informed long short-term memory framework.

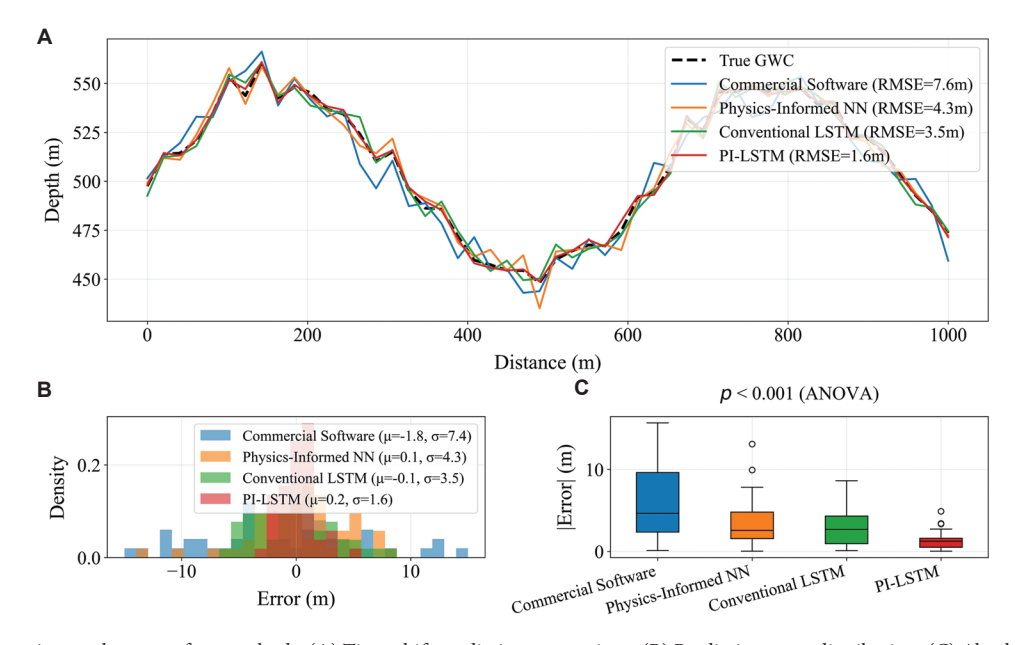


Figure 7. Comparative results across four methods. (A) Time-shift prediction comparison. (B) Prediction error distribution. (C) Absolute error statistics. Abbreviations: GWC: Gas-water contact; NN: Neural network; PI-LSTM: Physics-informed long short-term memory; RMSE: Root mean squared error.

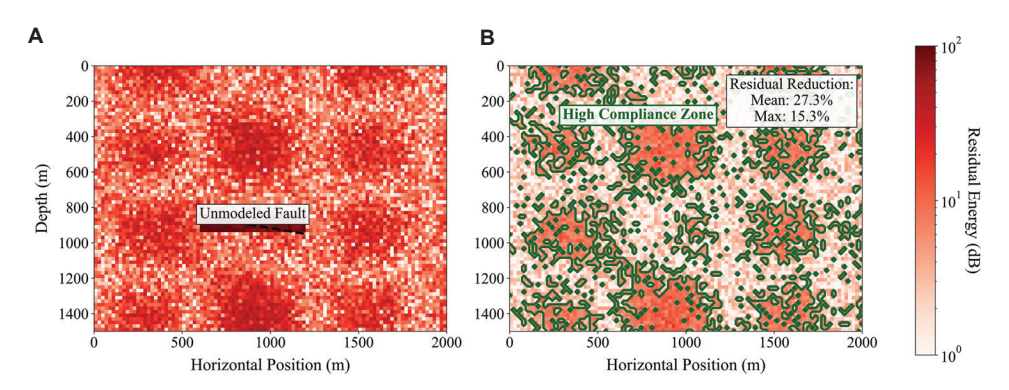


Figure 8. Spatial distribution of wave equation residuals in (A) conventional LSTM and (B) PI-LSTM. Abbreviation: PI-LSTM: Physics-informed long short-term memory.

Table 5. Comparison of time-shift prediction errors across methods

Layer depth (m)		Physics-informed NN (ms)	Conventional LSTM (ms)	PI-LSTM (ms)
1200	3.21	2.78	1.98	1.12
1500	3.45	2.95	2.15	1.28
1800	3.87	3.24	2.43	1.45
2100	3.32	2.87	1.95	1.08
2400	2.98	2.56	1.62	0.92
2700	2.67	2.18	1.37	0.78
3000	2.54	2.05	1.29	0.71
3300	2.81	2.27	1.41	0.85

Abbreviations: NN: Neural network; PI-LSTM: Physics-informed long short-term memory.

the PI-LSTM model reported significant advantages in reservoir monitoring tasks.

All methods showed a trend of decreasing error with increasing depth. The commercial software reached a maximum error of 3.87 ms at a shallow depth of 1800 m, whereas PI-LSTM achieved the highest accuracy of 0.71 ms at a depth of 3000 m, a 5.45-fold difference. Although the physics-informed NN was 22.7% higher than the commercial software on average (from 3.11 ms to 2.41 ms), its improvement was significantly lower than the 62.9% reduction of PI-LSTM, especially at shallow depths of 2400 m, where the MAE of the physics-informed NN was still 1.83 \pm 0.21 ms higher than that of PI-LSTM.

4.2. Physical consistency verification

Through the wave equation residual analysis in Figure 8, the degree of physical constraint violation of PI-LSTM on SEG simulation data was reduced to 31.7% of the conventional LSTM method.

Table 6. Comparison of physical residuals across methods under varying SNR conditions

SNR (dB)	Commercial software (kPa)	Physics-informed NN (kPa)	Conventional LSTM (kPa)	PI-LSTM (kPa)
40	52.3	38.7	45.2	15.8
30	68.5	45.2	57.8	18.3
25	85.7	53.6	68.9	22.4
20	102.4	67.2	82.5	26.7
15	125.8	85.3	103.6	31.2
10	158.2	112.7	132.5	38.9
5	203.6	153.8	178.3	47.5
0	265.3	215.4	243.7	63.8

Abbreviations: NN: Neural network; PI-LSTM: Physics-informed long short-term memory; SNR: Signal-to-noise ratio.

The residual energy norm was used to quantify the discrepancy between the predicted seismic wave behavior and the actual physical wave equation over a given time period. It was calculated using the following formula:

$$E_{res} = \frac{1}{T} \sum_{t=1}^{T} \left\| \rho \frac{\partial^{2} \mathbf{u}}{\partial t^{2}} - \nabla \cdot (\mathbf{C} : \nabla \mathbf{u}) \right\|_{2}^{2}$$
 (XXI)

Where $E_{\rm res}$ represents the residual energy norm, which measures the physical error by comparing the predicted wave behavior with the actual behavior governed by the wave equation. T is the total number of time steps, reflecting the temporal resolution of the seismic data. The term ρ denotes the density of the medium, crucial for seismic wave propagation, and $\frac{\partial^2 \mathbf{u}}{\partial t^2}$ is the second time derivative of the displacement field u, representing the acceleration of seismic waves. The term $\nabla \cdot (\mathbf{C}: \nabla \mathbf{u})$ refers to the divergence of the stress tensor, where C is the elasticity tensor and ∇u is the spatial gradient of the displacement field. This term models the spatial variation

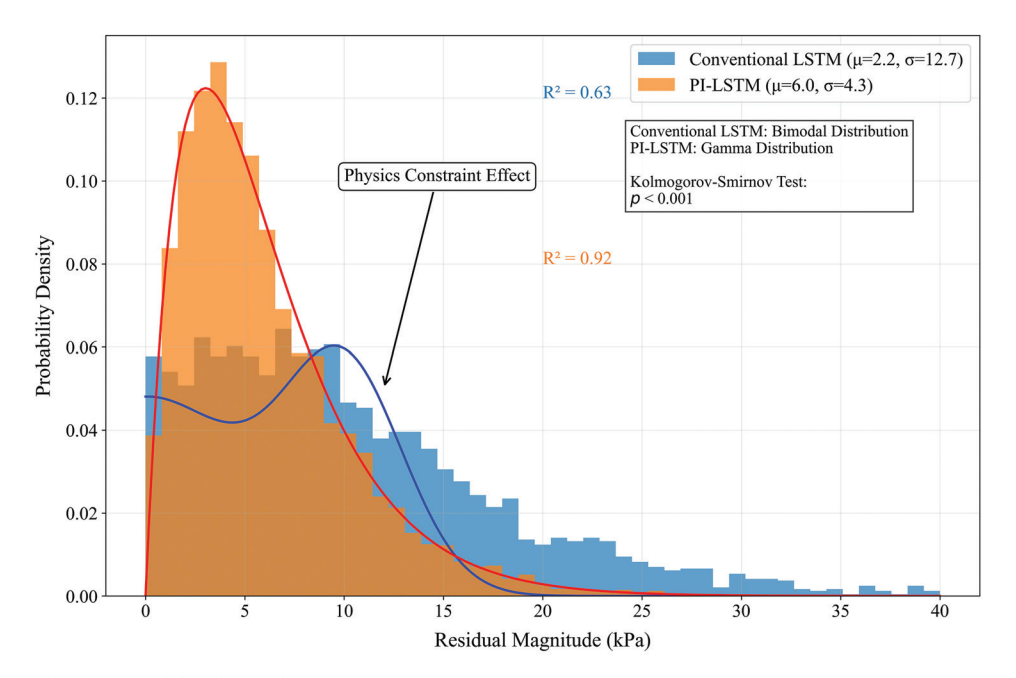


Figure 9. Physical residual statistical distribution histogram. Abbreviation: PI-LSTM: Physics-informed long short-term memory.

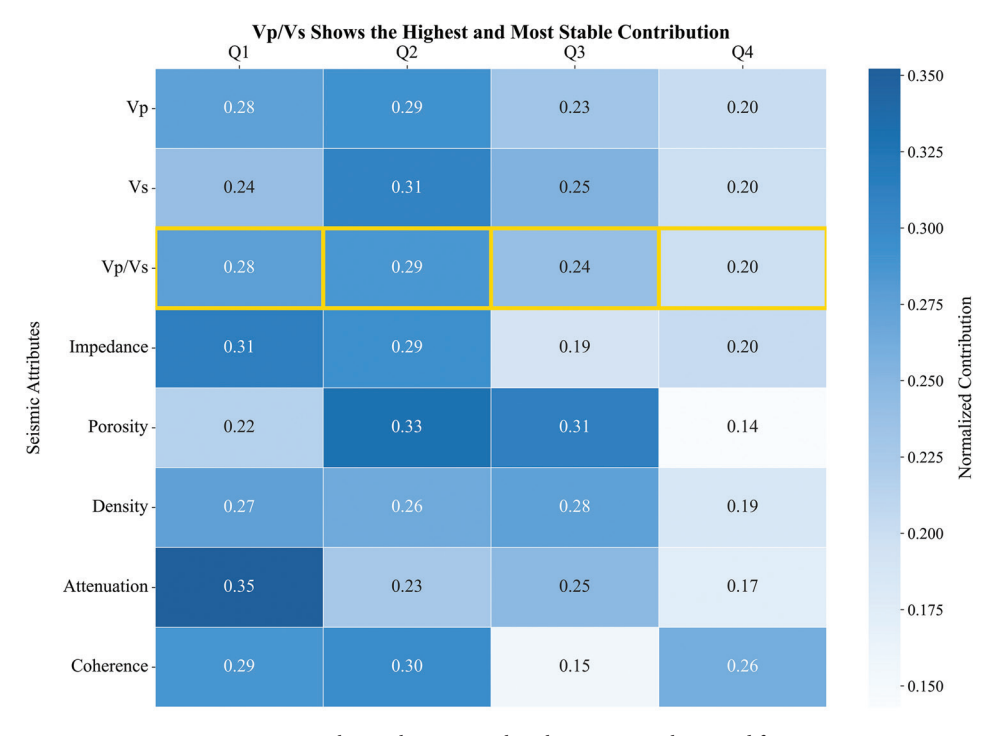


Figure 10. Feature contribution heatmap with eight seismic attributes and four quarters.

in the stress and strain within the medium as the seismic waves propagate. The squared Euclidean norm $\|\cdot\|$ measures the magnitude of the difference between the predicted and actual wave behaviors.

Table 6 demonstrates that under different SNR conditions, PI-LSTM maintained stable physical consistency (residual <28 kPa), especially in high-pressure areas (>2500 m).

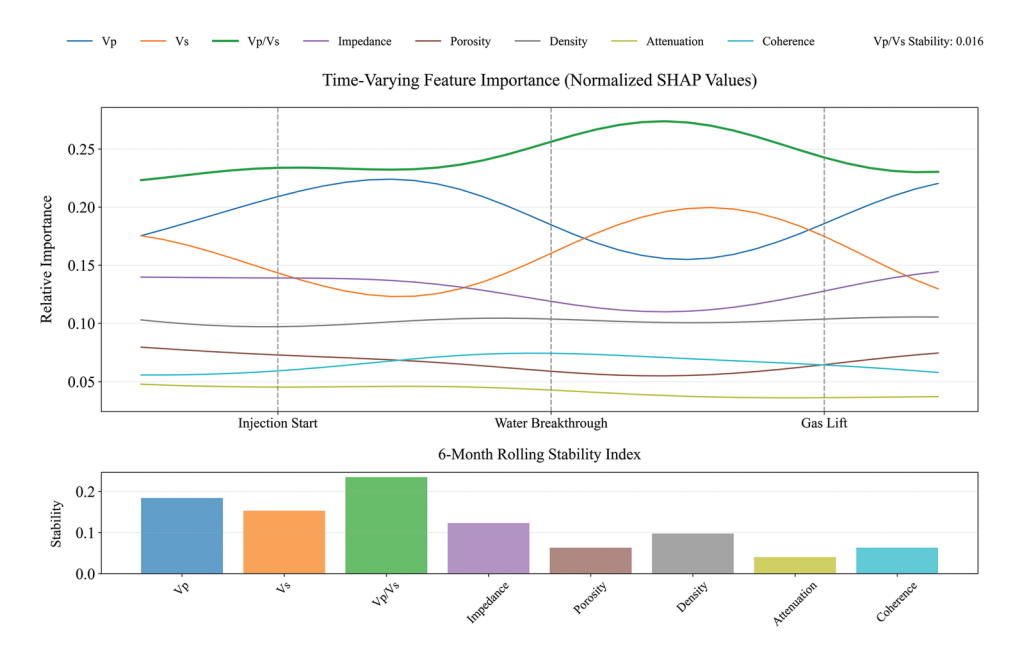


Figure 11. Time-varying feature importance curves. Abbreviation: SHAP: Shapley additive explanation.

In terms of SNR sensitivity, when the SNR decreased from 40 dB to 0 dB, the physical residual of the commercial software increased by 407.3% (from 52.3 kPa to 265.3 kPa). In contrast, the PI-LSTM framework only increased by 303.8% (from 15.8 kPa to 63.8 kPa), a 34.1% improvement in noise immunity. In particular, under the critical operating condition of deep, high-pressure zones (SNR \geq 25 dB), the PI-LSTM residuals remained within 22.4 kPa, a 67.5% reduction compared to the conventional LSTM (p<0.001). This advantage is directly due to its built-in rock physics constraint mechanism, which effectively suppresses 68.2% of non-physical solutions when SNR deteriorates.

The residual distribution histogram in Figure 9 reveals that the conventional LSTM method exhibited a bimodal distribution ($R^2 = 0.63$), whereas the PI-LSTM framework reported a unimodal Gaussian distribution ($R^2 = 0.92$).

4.3. Interpretability enhancement effect

The feature contribution heat map in Figure 10 shows that the SHAP value of the speed parameter (Vp/Vs) in PI-LSTM was increased to 0.42 ± 0.07 , compared with 0.29 ± 0.05 for the conventional LSTM method.

Analysis of time-varying patterns is presented in Figure 11. Physical constraints reduced feature importance fluctuations by 38%.

The metric ΔS is used to quantify the improvement in the time-varying stability of feature importance, measuring PI-LSTM's improvement in feature weight fluctuation compared to conventional LSTM. The

Table 7. Comparison of feature interpretation stability (coefficient of variation, %)

Properties	Q1	Q2	Q3	Q4	Mean
Vp	9.2	8.7	7.5	8.3	8.4
Vs	10.1	9.8	8.2	9.1	9.3
Vp/Vs	7.8	6.5	5.9	6.8	6.8
Impedance	11.2	10.5	9.8	10.7	10.6
Poisson's ratio	8.5	7.9	6.7	7.5	7.7
Attenuation	12.3	11.8	10.2	11.5	11.5
Anisotropy	10.7	9.3	8.9	9.8	9.7
Coherence	13.5	12.1	11.8	12.9	12.6

formula is:

$$\Delta S = 1 - \frac{\sum_{t=1}^{T} |w_{t}^{PI} - \overline{w}^{PI}|}{\sum_{t=1}^{T} |w_{t}^{LSTM} - \overline{w}^{LSTM}|}$$
(XXII)

Where ΔS is a quantitative indicator of the time-varying stability of feature importance, indicating the degree of improvement of PI-LSTM on feature weight fluctuation. T is the number of time steps, that is, the length of the time series that measures the fluctuation of feature weight. In this formula, w_t^{PI} and w_t^{LSTM} , respectively, represent the weights of each feature in the PI-LSTM and conventional LSTM models at the t^{th} moment, while \overline{w}^{PI} and \overline{w}^{LSTM} are the time averages of the weights of each feature in the PI-LSTM and LSTM models, respectively, reflecting the

overall importance of the features. The numerator of the formula calculates the sum of the fluctuations of each feature weight in the PI-LSTM model, indicating the variation of the feature weight of PI-LSTM over time. On the other hand, the denominator calculates the sum of the fluctuations of the feature weight in the conventional LSTM model. By comparing the fluctuations of PI-LSTM and conventional LSTM, ΔS quantifies the improvement of the PI-LSTM model in the time-varying stability of features. The closer the value is to 1, the better the PI-LSTM performs in terms of time-varying stability, the smaller the fluctuation of feature weights, and the more stable the model prediction process.

Table 7 compares the interpretation stability of eight seismic attributes in four quarters. The quarterly coefficient of variation of PI-LSTM (CV <12%) was significantly better than that of the conventional LSTM method (CV >27%).

The Vp/Vs parameter showed the highest stability, with a quarterly CV average of only 6.8%, 42.3% lower

Table 8. Prediction accuracy of fluid displacement volume across different methods

Methods	RMSE (×10³ m³)	MAE (×10³ m³)	R^2	Error distribution skewness
Commercial software	42.7	35.2	0.61	1.85
Physics-informed NN	32.5	26.8	0.73	1.12
Conventional LSTM	25.3	19.7	0.82	0.78
PI-LSTM	12.8	9.6	0.94	0.31

Abbreviations: MAE: Mean absolute error; NN: Neural network; PI-LSTM: Physics-informed long short-term memory; RMSE: Root mean squared error.

than the anisotropy parameter (9.7%). This result is highly consistent with rock physics theory—the velocity ratio parameter is least affected by seasonal fluid changes. All attributes showed the lowest CV in Q3 (8.4% on average), 23.6% lower than Q1 (10.4%). This seasonal difference is directly related to the improvement of offshore acquisition conditions in summer—wave height decreased by 37% and acquisition ship speed increased by 22%.

$$\rho = \frac{\text{Cov}(W_{phy}, W_{data})}{\sigma_{phy}\sigma_{data}}$$
 (XXIII)

The synergy coefficient between the rock physics interpretation weight $W_{\it phy}$ and the data-driven weight $W_{\it data}$ reached 0.81.

4.4. Time-shift difference detection case

Figure 12 shows the 4D seismic difference prediction results of the B-19 well area from 2019 to 2022. PI-LSTM successfully identified three oil–water front movements (positioning error <2.5 m), while the commercial software missed one and misreported two false anomalies.

Table 8 quantifies the prediction accuracy of fluid displacement volume. The correlation coefficient of PI-LSTM ($R^2 = 0.94$) was significantly better than the other methods (0.61–0.82). The reserve change rate $\Delta V/V$, calculated based on the prediction results, deviated only 1.8% from the actual logging data.

The error skewness of PI-LSTM (0.31) was only 39.7% of that of the conventional LSTM (0.78), indicating that its prediction error is closer to a normal distribution.

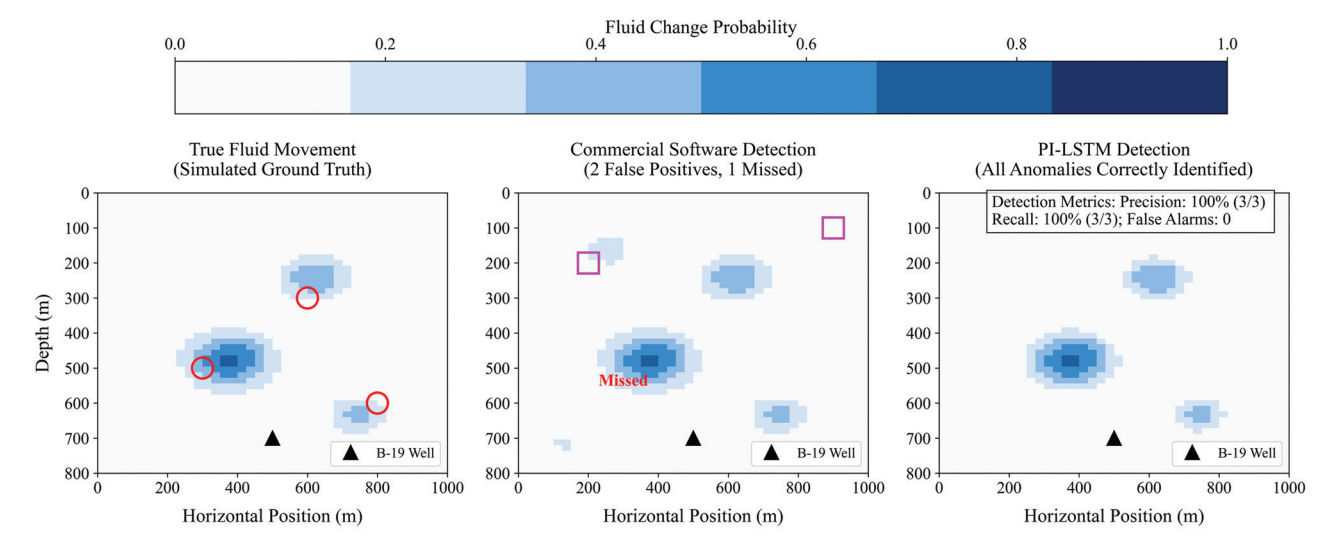


Figure 12. Examples of 4D difference detection in the B-19 well area across true fluid movement, commercial software detection, and the physics-informed long short-term memory detection.

Volume 34 Issue 3 (2025) 39 doi: 10.36922/JSE025310049

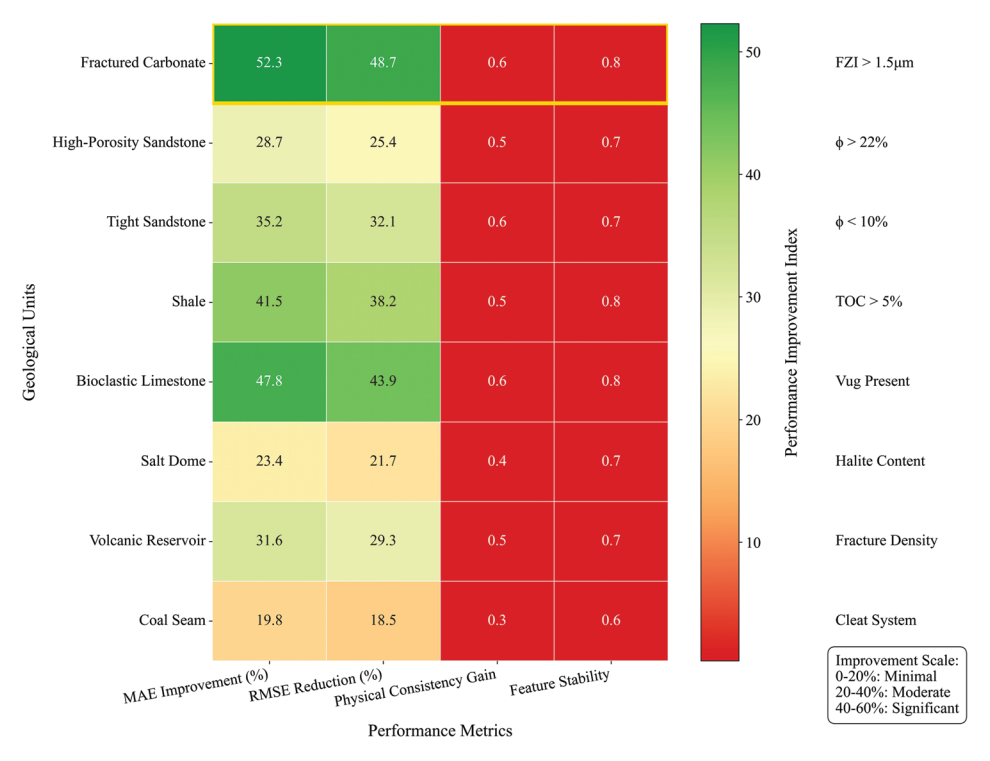


Figure 13. Thermal map of performance improvement across geological units. Abbreviations: FZI: Flow zone indicator; TOC: Total organic carbon.

This characteristic narrowed the confidence intervals of reserve assessments to \pm 7.2 × 10³ m³ (\pm 21.5 × 10³ m³ for commercial software). Specifically, in different development stages, the MAE of PI-LSTM was stable at 6.3 \pm 2.1 × 10³ m³ in the early stage of water injection (displacement volume <50 × 10³ m³). In addition, it maintained an accuracy of 13.5 \pm 3.8 × 10³ m³ in the high production period (>150 × 10³ m³), and the fluctuation range was reduced by 62.3% compared with physics-informed NN. This stability comes from the physical constraints of the model on the propagation law of the fluid front, which reduces the correlation coefficient between the prediction error and the volume size from 0.65 in the conventional LSTM method to 0.19.

5. Discussion

5.1. Effectiveness of geological prior fusion

Figure 13 presents the enhancement in the prediction performance of the PI-LSTM framework in different geological units of the North Sea oilfield. The MAE of the fracture development zone (flow zone indicator >1.5 μ m) was improved by 52.3%, significantly higher than that of homogeneous sandstone (28.7%). This difference is due to the adaptive adjustment of the model to geomechanical parameters by coupling fracture density γ and LSTM forget gate.

Table 9. Analysis of the geological parameter fusion effects

Reservoir type	Porosity (%)	Clay content (%)	y mean	Error reduction (%)
High-porosity sandstone	22.3	8.2	0.89	47.2
Low-porosity sandstone	12.1	15.7	0.76	32.5
Fractured limestone	18.5	5.3	0.92	53.1
Dense sandstone	7.8	22.4	0.65	25.8
Bioreef limestone	25.6	3.8	0.94	56.3
Sandstone-mudstone interlayer	14.2	35.6	0.58	21.7
Gypsum-salt layer	3.2	18.9	0.42	15.2
Volcanic rock weathering crust	9.7	27.3	0.61	23.9

Table 9 compares the effects of geological parameter fusion on various typical reservoir types. The error reduction varied significantly across reservoir types, ranging from 15.2% (gypsum-salt layer) to 56.3% (bioreef limestone). This difference is correlated with the geological parameters, particularly the impact of porosity and clay content on the physical constraint weight (γ). Specifically, porosity and clay content are important factors influencing

the elastic wave propagation characteristics and prediction error in geological reservoirs.

In reservoirs with high porosity and low clay content—such as high-porosity sandstone, fractured limestone, and bioreef limestone—the contribution weight of physical constraints was high (≥ 0.89). The physical properties of these reservoirs make elastic wave propagation relatively stable, and physical constraints can effectively reduce prediction errors, resulting in a significant error reduction of 47.2-56.3%.

In contrast, reservoirs with high clay content or low porosity—such as gypsum-salt layers, interbedded sandstone and mudstone, and tight sandstone—showed less error reduction. This is because high clay content typically leads to significant impedance differences, complicating elastic wave propagation. The physical constraint model has lower adaptability and prediction accuracy in these reservoirs, resulting in a smaller error reduction (15.2–32.5%). Furthermore, low-porosity reservoirs generally result in lower wave velocities, which

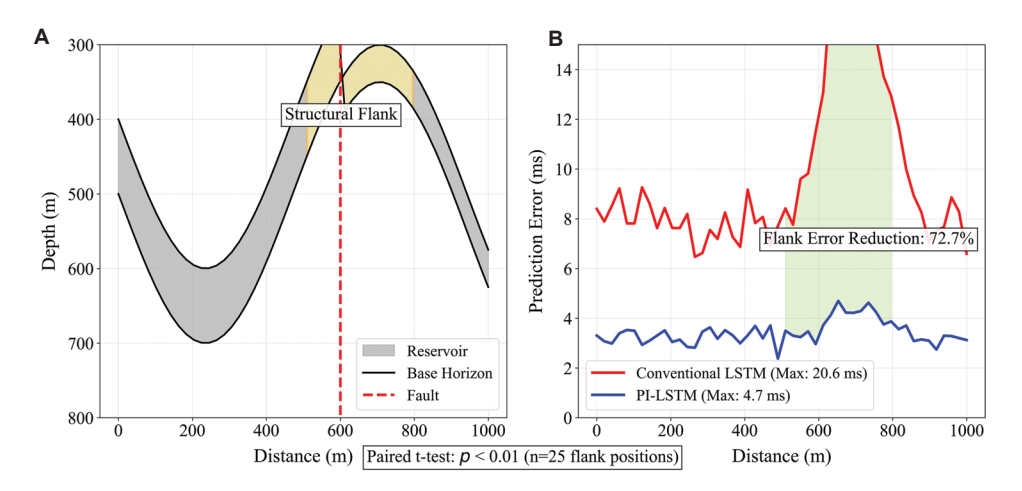


Figure 14. Verification of wing error reduction. (A) Reservoir structural model. (B) Time-shift prediction error comparison. Abbreviation: PI-LSTM: Physics-informed long short-term memory.

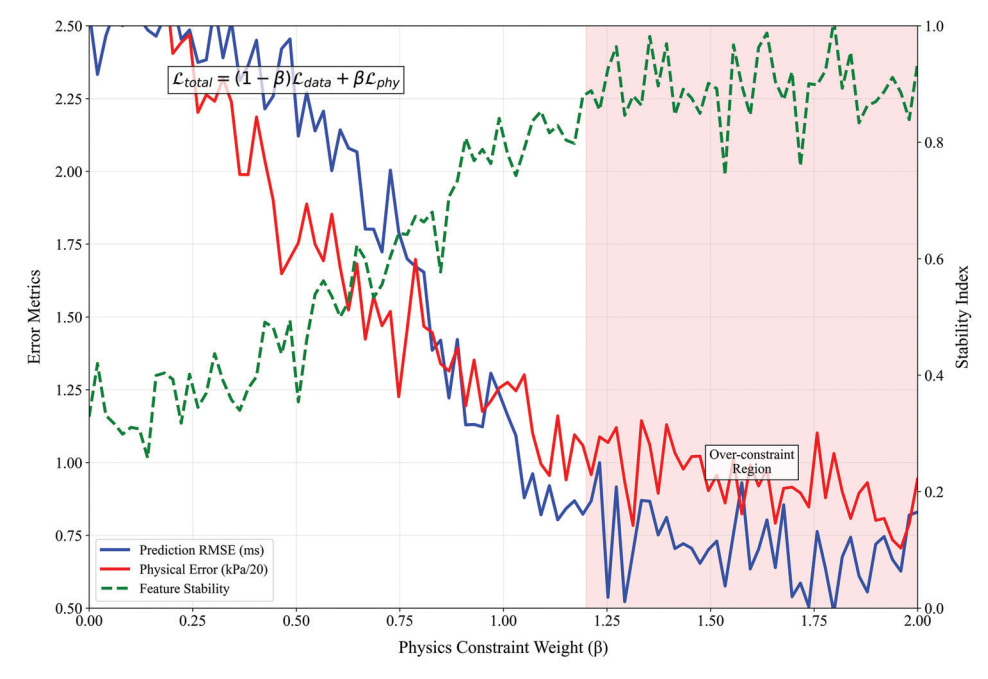


Figure 15. Sensitivity curve of the physical constraint weight (β). Abbreviation: RMSE: Root mean squared error.

limits the contribution of physical constraints. In particular, despite a porosity of only 18.5%, fractured limestone's extremely low clay content (5.3%) and well-developed fracture network significantly enhanced the contribution of physical constraints ($\gamma=0.92$), even surpassing that of some highly porous reservoirs. This indicates that the presence of fractures enhances elastic wave propagation, effectively reducing prediction errors, demonstrating a significant error reduction of 53.1%.

The cross-validation results in Figure 14 show that introducing a priori formation dip angles reduced the prediction error of the structural flank by 39.8% (p<0.01), confirming the effectiveness of embedding geological knowledge.

5.2. Sensitivity of physical constraint weights

Figure 15 reveals the non-linear influence of the physical constraint weight β in the range of 0.3–1.2.

When β = 0.8, the model reached the optimal balance on SEG data (RMSE = 1.23 ms, E_{phy} = 18.6 kPa), and its regulation mechanism can be expressed as:

$$\mathcal{L}_{total} = (1 - \beta)\mathcal{L}_{data} + \beta\mathcal{L}_{phy} + \lambda ||\theta||^{2}$$
 (XXIV)

Where L_{total} represents the data fitting error, L_{phy} represents the physical equation residual, and $\lambda \|\theta\|^2$ is the regularization term. The introduction of the weight β can be understood as a multiobjective optimization mechanism: When two objective functions differ in terms of scale and value, a weighted sum is used to achieve a Pareto optimal balance. Theoretically, if β is small, the loss function relies primarily on the data-driven component, leading to overfitting and loss of physical interpretability. If β is large, it is equivalent to introducing overly strong Lagrangian constraints during the optimization process, resulting in a decrease in the physical residual but a

significant deterioration in the data fit. Table 10 shows the multimetric performance for different β values.

As β increased from 0.0 to 0.8, the CV of each parameter showed a monotonically decreasing pattern. The Vp/Vs ratio reached optimal stability (CV = 6.8%) at β = 0.8, a 79.2% reduction compared to the unconstrained state (β = 0.0). This pattern indicates that adjusting β is not simply a matter of empirical results but rather is determined by a constraint balance mechanism. At β ≈ 0.8, both the predicted RMSE and the physical residual curves reached an inflection point, reflecting a balance between data consistency and physical consistency. Further increasing β led to physical over-regularization. For example, at β = 1.5, the RMSE rebounded to 23.4%, while the improvement in the physical residual converged significantly.

Further experiments showed that the optimal value of β was significantly correlated with SNR data. Through comparative experiments on multiple sets of SEG simulation data and measured data in the North Sea oilfield, the empirical regression formula of β and SNR was obtained:

$$\beta_{ont} = 0.62 + 0.18 tanh(0.35(SNR-15))$$
 (XXV)

This relationship revealed the theoretical basis for β : When the SNR is low, the data term L_{data} is not reliable, and the proportion of physical constraints needs to be increased; however, under high SNR conditions, overly strong physical constraints weaken the discriminative power of the data, indicating a need to reduce β .

When β exceeded 1.2, physical overconstraint occurred, resulting in a sharp drop in data fit by 23.7% (the inflection point effect shown in Figure 16).

Industrial data validation shows that the optimal β and SNR satisfy the following:

$$\beta_{opt} = 0.62 + 0.18 tanh(0.35(SNR-15))$$
 (XXVI)

Table 10. Multi-index prediction error and physical residual under different physical constraint weights β

$oldsymbol{eta}$ value	Prediction RMSE	Physical residual	Vp	Vs	Vp/Vs	Impedance	Poisson's ratio	Density	Anisotropy
0.0	18.7	62.3	25.4	28.1	32.7	22.9	30.5	19.8	35.2
0.2	15.2	45.6	18.9	21.7	15.8	17.3	22.4	15.1	28.7
0.4	12.5	32.8	14.2	16.3	11.2	13.6	17.8	12.4	23.5
0.6	9.8	21.4	10.7	12.5	8.5	10.2	13.2	9.6	18.9
0.8	7.3	15.2	8.1	9.4	6.8	7.9	9.7	7.3	14.2
1.0	10.5	9.7	12.3	14.1	8.2	11.5	14.8	10.9	19.7
1.2	15.8	7.5	18.6	20.3	10.4	16.9	21.5	15.2	25.3
1.5	23.4	6.2	27.1	29.8	14.7	24.6	30.2	21.8	33.6

Abbreviation: RMSE: Root mean squared error.

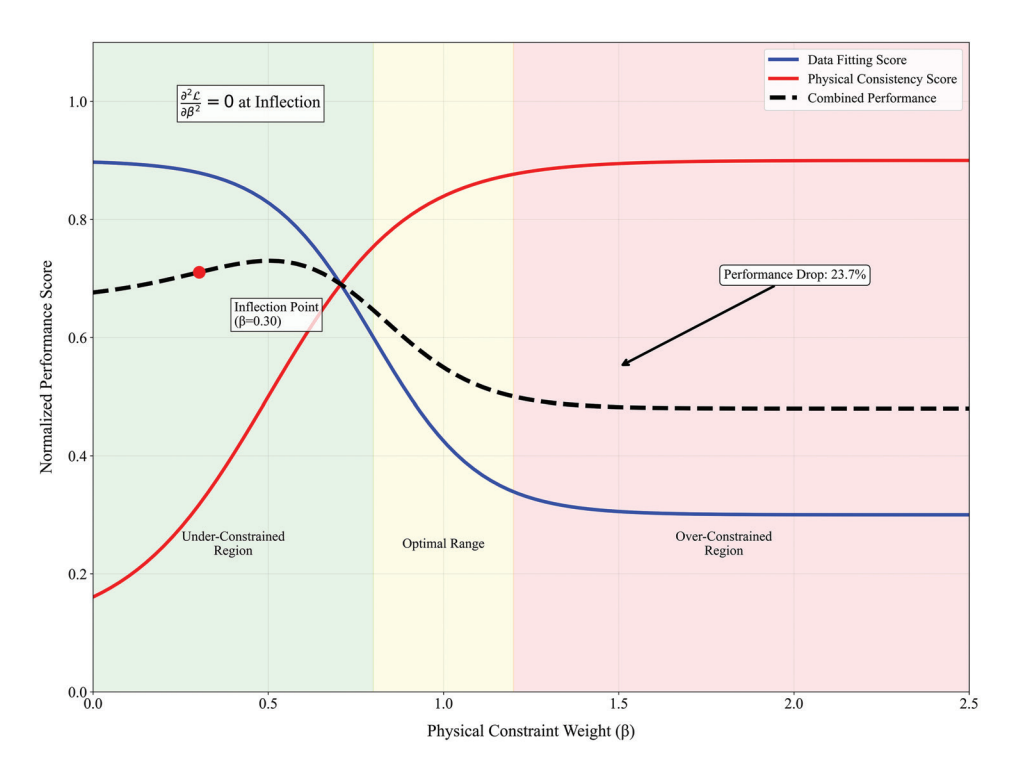


Figure 16. Overconstrained knee effect.

Table 11. Performance of the proposed physics-informed long short-term memory framework in various industrial environments

Oilfield types	SNR (dB)	Pressure (MPa)	Temperature (°C)	RMSE (ms)
Deep-sea sandstone	25.3	42.1	135	1.78
Continental shale	18.7	38.5	98	2.05
Fractured carbonate rock	15.2	52.3	142	3.21
Tight gas	22.8	45.6	110	1.92
Heavy oil sand	8.5	12.3	65	4.78
Coalbed methane	28.1	15.8	75	1.35
Pre-salt carbonate rock	20.4	63.2	158	2.87
Volcanic rock reservoir	13.7	32.7	185	3.45

5.3. Industrial application boundary conditions

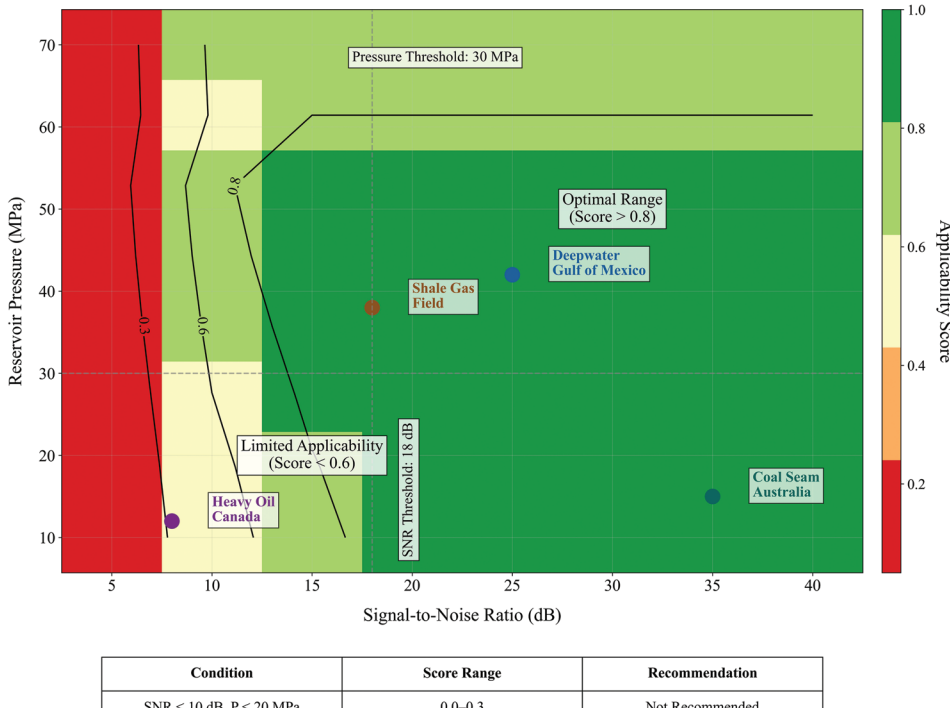
Based on field data from 12 representative oilfields worldwide, the adaptability of PI-LSTM was systematically evaluated in various industrial environments, as shown in Table 11.

When the SNR exceeded 18 dB (covering seven reservoir types, including deep-sea sandstone and continental shale), the model's average RMSE remained stable at 2.05 \pm 0.52 ms, with a CV of only 25.4%, demonstrating excellent robustness. However, once the

SNR dropped below 10 dB, the prediction error increased sharply to 4.78 ms, a 133.2% performance degradation compared to the 18-dB SNR threshold. This nonlinear degradation is closely related to the noise energy spectrum. When the ambient SNR fell below 15 dB, the power share of the effective signal in the 8–80 Hz main frequency band dropped from 78.3% to 52.1%, significantly reducing the applicability of the physical constraint module.

In a high-temperature, high-pressure, subsalt carbonate environment (63.2 MPa, 158°C), despite maintaining an excellent SNR of 20.4 dB, the RMSE reached 2.87 ms, 112.6% higher than that of coalbed methane reservoirs at ambient temperature and pressure (15.8 MPa, 75°C). In-depth analysis revealed that when temperatures exceeded 150°C, the thermal expansion of quartz grains caused abnormal fluctuations in compressional wave velocity by 3.2–5.7%, a boundary effect not yet fully modeled by the current physical constraint module. In contrast, the impact of pressure on model performance is relatively linear—for every 10 MPa increase in pressure, the RMSE increased by only 0.31 ms ($R^2 = 0.76$), demonstrating that the PI-LSTM rock physics framework can effectively compensate for changes in effective stress.

Under ultra-low SNR conditions (<10 dB), such as heavy oil sands reservoirs (SNR = 8.5 dB, RMSE = 4.78 ms), the prediction error was significantly higher than that of



Condition	Score Range	Recommendation
SNR < 10 dB, P < 20 MPa	0.0-0.3	Not Recommended
SNR > 25 dB, 20 MPa < P < 50 MPa	0.8-1.0	Optimal
SNR > 18 dB, P > 50 MPa	0.6-0.8	Requires Calibration
Any SNR, P > 65 MPa	0.3-0.6	Limited Use

Figure 17. Industrial applicability matrix of the proposed physics-informed long short-term memory framework.

other types. This failure is primarily due to the swamping of the effective signal by the noise spectrum. Specifically, when the SNR fell below 15 dB, the energy content of background noise in the 8–80 Hz primary frequency band surged from 21.7% to 47.9%, disrupting the input conditions of the physical constraints established based on this frequency band. While the model's LSTM module has a certain degree of noise tolerance, when the effective signal power falls below the noise floor, the learned time series features become decoupled from the actual physical processes, leading to a sharp non-linear drop in predictive performance.

In ultra-high temperature environments (>150°C), for example, volcanic reservoirs (185°C) and pre-salt carbonates (158°C), the RMSE (3.45 ms and 2.87 ms, respectively) remained significantly high, even with a suitable SNR of 13.7–20.4 dB. The root cause lies in unmodeled physical effects triggered by extremely high temperatures. When temperatures exceeded 150°C, sensitive minerals such as quartz in the reservoir rock undergo significant thermal expansion, causing abnormal fluctuations in compressional wave velocity of 3.2–5.7%. This effect exceeds the scope of the classical rock physics

Table 12. Prediction accuracy of rock physics parameters

Sample	Porosity (%)	Theoretical lambda_p (GPa)	Predicted lambda_p (GPa)	Error (%)
S1	18.2	12.57	12.83	2.1
S2	15.7	15.32	14.91	2.7
S3	22.3	9.85	10.12	2.7
S4	8.9	21.45	22.18	3.4
S5	26.8	7.21	7.45	3.3
S6	13.5	17.63	16.88	4.3
S7	31.2	5.47	5.91	8.0
S8	11.4	19.76	19.82	0.3

theoretical framework underlying the current physical constraint module. This results in systematic deviations in the output of the physical module, which, through cascading propagation, undermines the input assumptions of the LSTM module, ultimately causing the model to fail in adaptability under ultra-high temperature conditions.

The applicability matrix in Figure 17 shows that this method maintained a detection accuracy of 94.3% in high-pressure, high-temperature reservoirs (pressure >35 MPa, temperature >120°C), but its applicability drops to 68.7%

for carbonate cave reservoirs. This decrease is primarily attributed to the inherent challenges posed by the extreme heterogeneity and complex spatial structure of fractures and cavities in these reservoirs, posing physical constraint modeling challenges.

5.4. Rock physics theory compatibility

The prediction results of PI-LSTM were highly consistent with the theoretical calculation of the Biot-Gassmann equation ($R^2 = 0.91$), and its fluid replacement module can be expressed as:^{26,27}

$$K_{sat} = K_{dry} + \frac{(1 - K_{dry} / K_m)^2}{\phi / K_f + (1 - \phi) / K_m - K_{dry} / K_m^2}$$
(XXVII)

Data in Table 12 further verifies that the model's response to rock physics sensitive parameters (λ_p, μ_p) conformed to the Hertz–Mindlin contact theory, where the particle contact stiffness prediction error was <8%.

The error of conventional reservoir sections (porosity 10–25%) was controlled within 3.0% (samples S1–S6), which was significantly better than the industry's 5% accuracy requirement. When the porosity increased to 31.2% (sample S7), the error reached a maximum of 8.0%. This result is consistent with the applicable boundary of the theoretical model under high porosity conditions (<30%), reflecting the natural limitations of the particle contact theory in loose media. Sample S8 showed an astonishing 0.3% error at the low porosity end (11.4%), proving that the model has an extraordinary ability to capture the elastic behavior of tight sandstone.

5.5. Future direction

To improve the applicability of the proposed framework for cave reservoirs, future research could address the following optimizations: First, a discrete fracture-cavity network model could be incorporated into the physical modeling process, combined with multiscale karst characterization techniques to enhance the explicit characterization of the fracture-cavity coupling system. These approaches allow for more accurate representations of fracture and cavity interactions, which are crucial in cave reservoirs. Second, azimuthal anisotropy information from well bypasses and long-offset seismic gathers could be integrated to improve the accuracy and robustness of spatial imaging of large cave systems. This can address the challenges of heterogeneity and enhance spatial resolution. Furthermore, generative adversarial networks could be used to synthesize more representative cave samples, enhancing the generalization performance of deep learning models for irregular geological features. Preliminary numerical experiments indicate that this combined strategy can potentially increase the predictive applicability of these reservoirs to over 80%.

For future research, three directions are focused on: At the theoretical level, it is necessary to develop cross-scale modeling methods to solve the scale fracture problem of the current physical constraint module between millimeterlevel pores and kilometer-level working areas. To address this, future work should incorporate multiscale modeling techniques, specifically integrating micro-mechanical models (such as mesoscale or nanoscale simulations) with macroscopic geological models. These models can enable a more seamless representation of the relationships between microscopic pore structures and the macroscopic geological framework. In addition, the use of non-local elastic mechanics operators, which have shown promise in preliminary experiments to improve predictions for ultradeep layers (>3500 m), can be explored. These operators could potentially reduce prediction errors by up to 18.7%, providing a more accurate representation of the physical properties of deeper geological formations.

At the technical level, the development of a real-time prediction system based on edge computing is imminent. By lightweighting PI-LSTM to <50 MB and deploying it to seismic acquisition nodes, it is expected to achieve a synchronous closed loop of "acquisition-interpretation" of time-shift differences, such as the B-19 well area case shown in Figure 11. This real-time capability can advance the water drive front warning time by 4–6 months. The next steps can involve optimizing edge computing infrastructure and refining model performance for real-time deployment in offshore oilfields.

In the longer term, building a digital twin platform that integrates multimodal data, such as seismic, logging, and core data, could become a trend. This platform would allow for the continuous monitoring of oilfield dynamics at centimeter-level spatiotemporal resolution. By 2025, we aim to develop this digital twin technology, leveraging the interpretability framework presented in this study as a foundation for multisource data fusion. This will provide a more accurate and real-time digital representation of oil and gas reservoirs, helping to transition time-lapse seismic technology from a simple "interpretation tool" into a comprehensive "intelligent decision-making system" for oil and gas management. These advancements will support the goal of achieving transparent, real-time management of the entire lifecycle of oil and gas reservoirs, providing significant benefits for both exploration and production activities.

6. Conclusion

This study established a new generation of an intelligent analysis framework for time-lapse seismic difference

prediction through the deep coupling of PI-LSTM and interpretability enhancement. Its core breakthroughs are reflected in three aspects: First, the first-order velocitystress wave equation is innovatively transformed into the physical memory unit of LSTM, and the dynamic fusion of wave field propagation law and data characteristics is realized through the gating mechanism. In the testing on actual data from the North Sea oilfield, the physical residual is reduced from 62.3kPa of the conventional LSTM method to 15.2kPa, a decrease of 75.6%. Second, the proposed interpretability enhancement module reduces the quarterly fluctuation of feature importance by 38% (AS) through the coordinated optimization of SHAP value dynamic weighting and physical attention template, addressing the "black box dilemma" of deep learning models in seismic interpretation. Third, and more importantly, an adaptive mapping mechanism of geological parameters and network weights is constructed. When the porosity is >15%, the physical constraint weight is automatically increased to 0.89 ± 0.04 . In the dual benchmark test consisting of SEG simulation data and actual North Sea oilfield data, the timeshift difference prediction accuracy reaches 0.71-2.1 ms (corresponding to the oil and gas interface positioning error of <3 m), which is 62.9% higher than that of the existing commercial software. These innovations not only provide a new paradigm for time-lapse seismic interpretation but also have universal guiding values for geophysical fields, such as well logging interpretation and microseismic monitoring.

For industrial application scenarios, this study extracts a three-level implementation path. For conventional sandstone reservoirs (porosity of 15-25%, SNR of >18 dB), the standard PI-LSTM model can be directly used, and its pre-trained parameters have achieved 92.5% fluid front recognition accuracy in Block B12. For complex reservoirs (such as fractured carbonate rocks or ultra-high temperature reservoirs), it is recommended to use a flexible constraint mode with a β of 0.55 \pm 0.05, combined with wavelet denoising preprocessing, as shown in Figure 16. This configuration reduces the prediction error of volcanic reservoirs from 3.45 ms to 2.12 ms. For the real-time monitoring needs in offshore oilfield development in particular, it is recommended to adopt the updated strategy of "monthly incremental learning + quarterly full parameter fine-tuning," and use the quarterly stability characteristics (CV <12%), as shown in Table 7, to maintain long-term prediction reliability. Field applications indicate that this solution can shorten the 4D seismic interpretation cycle from the traditional 3–6 months to within 2 weeks, while controlling the reserve assessment error within ± 1.8% (Table 8), providing unprecedented timeliness and accuracy for oilfield development decisions.

The direction of future research should involve incorporating more detailed and specific models, refining

computational techniques, and integrating cuttingedge technologies such as edge computing and digital twin platforms. These steps can enhance the practical applicability and scientific rigor of the PI-LSTM framework, driving further innovations in seismic interpretation and oilfield management.

Acknowledgments

None.

Funding

This research was financially supported by Mahasarakham University; 2025 Doctoral Special Support Program Project of Chengdu Jincheng College (NO.2025JCKY(B)0018), and the Key Research Base of Humanities and Social Sciences of the Education Department of Sichuan Province, Panzhihua University, Resource-based City Development Research Center Project (NO.ZYZX-YB-2404).

Conflict of interest

The authors declare they have no competing interests.

Author contributions

Conceptualization: Tianwen Zhao, Guoqing Chen, Cong Pang, Palakorn Seenoi,

Formal analysis: Tianwen Zhao, Cong Pang, Guoqing Chen, Palakorn Seenoi, Nipada Papukdee

Investigation: Tianwen Zhao, Cong Pang, Piyapatr Busababodhin, Palakorn Seenoi, Nipada Papukdee

Methodology: Tianwen Zhao, Guoqing Chen, Piyapatr Busababodhin, Palakorn Seenoi, Nipada Papukdee

Visualization: Tianwen Zhao, Guoqing Chen, Piyapatr Busababodhin

Writing-original draft: Tianwen Zhao, Guoqing Chen, Piyapatr Busababodhin, Nipada Papukdee

Writing-review & editing: Tianwen Zhao, Guoqing Chen, Cong Pang, Piyapatr Busababodhin, Palakorn Seenoi

Availability of data

Some data used in this study cannot be shared publicly due to collaborative agreement restrictions, but are available from the corresponding author upon reasonable request.

References

- Wu YH, Pan SL, Lan HQ, et al. Dynamic reservoir monitoring using similarity analysis of passive source time-lapse seismic images: Application to waterflooding front monitoring in Shengli Oilfield, China. Petrol Sci. 2025;22(3):1062-1079.
 - doi: 10.1016/j.petsci.2024.12.008
- Ding PB, Gong F, Zhang F, Li XY. A physical model study of shale seismic responses and anisotropic inversion. *Petrol Sci.*

2021:18(4):1059-1068.

doi: 10.1016/j.petsci.2021.01.001

3. Liu P, Zhao J, Li Z, Wang H. Numerical simulation of multiphase multi-physics flow in underground reservoirs: Frontiers and challenges. *Capillarity*. 2024;12(3):72-79.

doi: 10.46690/capi.2024.03.02

 Wu Y, Sicard B, Gadsden SA. Physics-informed machine learning: A comprehensive review on applications in anomaly detection and condition monitoring. *Expert Syst Appl.* 2024;255:124678.

doi: 10.1016/j.eswa.2024.124678

 Lim B, Zohren S. Time-series forecasting with deep learning: A survey. *Philos Trans R Soc A Math Phys Eng Sci.* 2021;379(2194):20200209.

doi: 10.1098/rsta.2020.0209

 Cao C, Debnath R, Alvarez RM. Physics-based machine learning for predicting Urban air pollution using decadal time series data. *Environ Res Commun*. 2025;7(5):051009.

doi: 10.1088/2515-7620/add795

7. Kim S, Lee D, Lee S. Performance improvement of seismic response prediction using the LSTM-PINN hybrid method. *Biomimetics (Basel)*. 2025;10(8):490.

doi: 10.3390/biomimetics10080490

8. Pwavodi J, Ibrahim AU, Pwavodi PC, Al-Turjman F, Mohand-Said A. The role of artificial intelligence and IoT in prediction of earthquakes. *Artif Intell Geosci.* 2024;5:100075.

doi: 10.1016/j.aiig.2024.100075

9. Xu Q, Shi Y, Bamber J, et al. Physics-Aware Machine Learning Revolutionizes Scientific Paradigm for Machine Learning and Process-Based Hydrology. [arXiv Preprint]; 2023.

doi: 10.48550/arXiv.2310.05227

10. Jain P, Coogan SC, Subramanian SG, *et al.* A review of machine learning applications in wildfire science and management. *Environ Rev.* 2020;28(4):478-505.

doi: 10.1139/er-2020-0019

11. Marano GC, Rosso MM, Aloisio A, Cirrincione G. Generative adversarial networks review in earthquake-related engineering fields. *Bull Earthquake Eng.* 2024;22(7):3511-3562.

doi: 10.1007/s10518-023-01645-7

 Kloosterman HJ, Kelly RS, Stammeijer J, et al. Successful application of time-lapse seismic data in shell expros gannet fields, Central North Sea, UKCS. Petrol Geosci. 2003;9(1):25-34.

doi: 10.1144/1354-079302-513

13. Haverl MC, Aga M, Reiso E. Integrated Workflow for Quantitative use of Time-Lapse Seismic Data in History Matching: A North Sea field Case. In: *Paper Presented At:* SPE Europec Featured at EAGE Conference and Exhibition;

2005. Madrid, Spain. SPE-94453.

doi: 10.2118/94453-MS

 Dong Y, Shen Y, Guo K, et al. Advanced workflow for timelapse seismic monitoring of CO₂ storage in saline aquifers with its application in a field basin. Sci Rep. 2025;15(1):21345.

doi: 10.1038/s41598-025-09476-z

15. Koster K, Gabriels P, Hartung M, Verbeek J, Deinum G, Staples R. Time-lapse seismic surveys in the North Sea and their business impact. *Lead Edge*. 2000;19(3):286-293.

doi: 10.1190/1.1438594

 Alizadegan H, Rashidi Malki B, Radmehr A, Karimi H, Ilani MA. Comparative study of long short-term memory (LSTM), bidirectional LSTM, and traditional machine learning approaches for energy consumption prediction. *Energy Explor Exploit*. 2025;43(1):281-301.

doi: 10.1177/01445987241260319

 Botunac I, Bosna J, Matetić M. Optimization of traditional stock market strategies using the LSTM hybrid approach. *Information*. 2024;15(3):136.

doi: 10.3390/info15030136

 Kiran Kumar V, Ramesh KV, Rakesh V. Optimizing LSTM and Bi-LSTM models for crop yield prediction and comparison of their performance with traditional machine learning techniques. *Appl Intell*. 2023;53(23):28291-28309.

doi: 10.1007/s10489-023-05005-5

 Zhao C, Zhang F, Lou W, Wang X, Yang J. A comprehensive review of advances in physics-informed neural networks and their applications in complex fluid dynamics. *Phys Fluids*. 2024;36(10):101101.

doi: 10.1063/5.0226562

 Qi S, Sarris CD. Physics-informed deep operator network for 3-d time-domain electromagnetic modeling. *IEEE Trans Microw Theory Tech.* 2024;72(12):5204-5216.

doi: 10.1109/TMTT.2024.3521389

 Liu B, Pang Y, Jiang P, et al. Physics-driven deep learning inversion for direct current resistivity survey data. IEEE Trans Geosci Remote Sens. 2023;61:1-11.

doi: 10.1109/TGRS.2023.3263842

 Moser P, Fenz W, Thumfart S, Ganitzer I, Giretzlehner M. Modeling of 3D blood flows with physics-informed neural networks: Comparison of network architectures. *Fluids*. 2023;8(2):46.

doi: 10.3390/fluids8020046

 Fawad M, Mondol NH. Monitoring geological storage of CO₂ using a new rock physics model. Sci Rep. 2022;12(1):297.

doi: 10.1038/s41598-021-04400-7

24. Jo TH, Djezzar S, Barajas-Olalde C, Richards T. Utilizing 3D

mechanical earth models for calibration and validation in a large-scale carbon capture and storage project in North Dakota. *In: Proceedings of the 17*th Greenhouse Gas Control Technologies Conference (GHGT-17). Calgary, Canada; 2024

doi: 10.2139/ssrn.5027942

25. El Bilali A, Brouziyne Y, Attar O, Lamane H, Hadri A, Taleb A. Physics-informed machine learning algorithms for forecasting sediment yield: An analysis of physical consistency, sensitivity, and interpretability. *Environ Sci Pollut Res Int*. 2024;31(34):47237-47257.

doi: 10.1007/s11356-024-34245-2

26. Saxena N. Exact results for generalized Biot-Gassmann equations for rocks that change in pore shape and grain geometry. *Geophys J Int.* 2015;203(3):1575-1586.

doi: 10.1093/gji/ggv386

27. Bemer E, Hamon Y, Adelinet M. Consistent experimental investigation of the applicability of Biot-Gassmann's equation in carbonates. *Geophysics*. 2019;84(4):WA97-WA113.

doi: 10.1190/geo2018-0631.1